



POLITECNICO
MILANO 1863

SCUOLA DI INGEGNERIA INDUSTRIALE
E DELL'INFORMAZIONE

Towards OAM Light Generation with Femtosecond Laser Written Waveguides Circuits

TESI DI LAUREA MAGISTRALE IN
ENGINEERING PHYSICS
INGEGNERIA FISICA

Author: **Omer Ahmed Siddig Altaher**

Student ID: **952608**
Advisor: **Dr. Roberto Osellame**
Co-advisor: **Dr. Andrea Crespi**
Academic Year: **2021-22**

Abstract

Applications with a focus on the orbital angular momentum (OAM) of classical and quantum light states have significant potential due to the ability to encode information in multi-dimensional degrees of freedom. Such states form discrete high-dimensional quantum systems, also called qudits, which in principle can have any number of discrete levels. As a result, this increases the amount of information that a single quantum carrier can hold. To this purpose, an integrated photonic circuit could be employed which, in the terminal part, consists of waveguides passing from the planer configuration to the polygonal one.

An OAM beam could be produced exploiting the far-field distribution emitted by the outputs of an array of N waveguides, placed at the vertices of a regular polygon, endowed with a cyclical phase.

In this thesis, the specifications and the design of the integrated circuit to transform eight uncoupled waveguides into an octagonal cross section are presented. The design of the circuit fully exploits the unique potentialities of the femtosecond laser micromachining technique, which we use to realize three-dimensional waveguides.

We describe in detail the fabrication of the waveguides together with their optical characterization. In the final device, the parasitic coupling among the waveguides was quenched by controlling their propagation constant in the region where they are brought close together to produce the final octagonal structure. The optimal devices that have been achieved have more than 95% of the input power remaining in the same arm, while the interaction distance was as low as $6.6 \mu\text{m}$ between the waveguides.

Abstract in Italiano

Condizionare le informazioni sul momento angolare orbitale (OAM) degli stati di luce classici e quantistici, presenta un potenziale significativo grazie alla possibilità di sfruttare gradi di libertà a molte dimensioni. In fatti, tali stati formano sistemi quantistici discreti chiamati anche qudits, che in linea di principio possono avere un numero qualsiasi di livelli. Di conseguenza, il qudit amplia la quantità di informazioni che una singola particella quantistica può portare.

Un fascio OAM potrebbe essere prodotto sfruttando la distribuzione di campo lontano, prodotta dalle uscite di un array di N guide d'onda poste ai vertici di un poligono regolare, e dotate di una fase ciclica. Un circuito ottico integrato che svolga questa funzione presenta una sezione terminale, in cui le guide d'onda sono condotte da una configurazione planare alla geometria poligonale desiderata.

In questa tesi vengono presentate le specifiche e il progetto del circuito integrato per trasformare otto guide d'onda disaccoppiate in una sezione ottagonale. Il progetto del circuito sfrutta appieno le potenzialità uniche della tecnica di microlavorazione laser a femtosecondi, utilizzata per realizzare guide d'onda tridimensionali.

Viene descritta in dettaglio la fabbricazione delle guide d'onda e la loro caratterizzazione ottica. L'accoppiamento parassita tra le guide d'onda, nella regione in cui vengono avvicinate per produrre la struttura ottagonale finale, è stato fortemente attenuato controllandone la costante di propagazione migliori dispositivi ottenuti hanno più del 95% della potenza in ingresso che rimane nello stesso braccio, mentre la distanza di interazione tra le guide d'onda è di soli $6.6\mu\text{m}$.

Contents

Abstract	i
Abstract in Italiano	iii
Contents	v
Introduction	1
1 Orbital Angular Momentum for Quantum Information	3
1.1. Maxwell's Equations and Electromagnetic Waves	3
1.1.1. Electromagnetic Field	4
1.1.2. The polarization.....	5
1.1.3. Waveguide Structure	5
1.1.4. Gaussian Beam	6
1.1.5. Laguerre-Gauss mode (LG)	7
1.2. Quantization of The Electromagnetic Field.....	7
1.3. The Angular Momentum.....	9
1.4. Orbital Angular Momentum of Light	10
1.5. Ring Core Optical Fiber	13
1.6. Quantum Photonics.....	17
1.7. Quantum Information and Higher Dimensional Quantum States.....	21
2 Femtosecond Laser Written Waveguides	25
2.1. Femtosecond Pulse and Matter Interaction.....	25
2.1.1. Non-Linear Absorption.....	25
2.1.2. Dielectric Response and The Permanent Modification of The Refractive Index	27
2.2. Waveguide Writing	27
2.2.1. Writing Configuration	28
2.2.2. The Repetition Rate and the Thermal Effect.....	28
2.2.3. Annealing Process.....	29
2.3. State of the Art of 3D Devices	30
2.3.1. Passive Integrated Photonics Circuits	30
2.3.2. Reconfigurable Photonic devices	33
2.3.3. Thermal Phase Shifters	33
2.4. Manipulation of OAM of Light in Femtosecond laser written waveguides	34

2.5.	Waveguides at Octagonal 2D Cross Section	35
3	Experimental Methods	38
3.1.	FLM Apparatus	38
3.1.1.	The Laser System	38
3.1.2.	Motion stages	39
3.2.	Post-Processing and Visual Inspection	39
3.3.	Optical Characterization Method	40
3.3.1.	Waveguide's Mode Profile	41
3.3.2.	Losses Characterization	41
4	Optimization of Waveguides and Directional Couplers	43
4.1.	Optimization of Waveguides	43
4.1.1.	Coupling and Propagation Losses Optimization	43
4.1.2.	Characterization of Bending Losses	46
4.2.	Directional Couplers Characterization	47
4.2.1.	Coupled mode theory	47
4.2.2.	Directional Couplers	48
5	Fabrication of Three-Dimensional Waveguides in Octagonal Configuration	53
5.1.	The Geometrical Design of the Device	53
5.2.	Propagation of Eight-Waveguides	54
5.3.	Fabrication of the devices	55
5.4.	Characterization of the Devices	57
6	Conclusion	62
	Bibliography	63
	List of Figures	73
	List of Tables	75
	Acknowledgments	79

Introduction

Photons are a convenient choice for communication as they can be transported efficiently in free space and fiber over long distances with low loss. The ability to encode information in spatial degrees of freedom folds a considerable potential for a variety of applications, with a particular focus on the orbital angular momentum of classical and quantum light states. Such states form discrete high-dimensional quantum systems, also called qudits. A qudit is encoded on a quantum particle which is not limited to two states but in principle can have any number of discrete levels. As a result, the qudit enlarges the amount of information that a single quantum carrier can hold.

The fundamental property of photons carrying OAM is the presence of the helical phase factor $e^{il\varphi}$, where φ is the azimuthal coordinate that is in the plane transverse to the propagation direction. OAM beams can be produced using bulk optics components, which however are limited to shaping the wavefront of a free-space propagating light beam. Therefore, interfacing OAM beams with fiber networks and integrated optical circuits encounters stability and alignment problems, which limits the exploitation of these methods in the applications. On the other hand, integrated optical technology offers great advantages in terms of stability and robustness.

Femtosecond laser micromachining is an important technique for three-dimensional integrated photonic circuit realization. This approach enables the direct and efficient fabrication of high-quality three-dimensional waveguides without the need for any lithographic steps or clean-room laboratories. Moreover, femtosecond laser written-waveguides made in glass can be perfectly mode-matched to the optical fibers.

According to a published theoretical study, by researchers of the Physics Department of Politecnico di Milano. An OAM beams could be produced exploiting the far-field distribution produced by the outputs of an array of N waveguides, placed at the vertices of a regular polygon, endowed with a cyclical phase.

The required integrated circuit to generate an optical beam possessing OAM this scenario could be divided into three different sections. A power splitting device, such as a star coupler, could be used in the first stage, to divide the input light from the fiber into several branches with the required amplitude ratios and cyclical phase terms. The phase terms of each waveguide could be tuned, thus correcting experimental imperfections, using an array of phase shifters (such as thermo-optic devices) in the second part. The third section transforms the waveguides from a planar arrangement to the required two-dimensional cross-section, bringing each waveguide to its final position.

Note that the three-dimensional capabilities of femtosecond laser writing technology enable the fabrication of arrays of single-mode waveguides placed at the vertices of a regular polygon structure. Moreover, the output mode of each waveguide is a nearly-gaussian mode.

This work aims to engineer and realize the third section of the device, which transforms eight waveguides from a planar configuration to the vertices of a regular octagonal cross-section.

Parasitic coupling among neighboring waveguides, in the region where they are brought close together, needs to be carefully investigated in order to produce the final octagonal structure.

In this thesis we will present the specifications and design of the integrated circuit to transform eight uncoupled waveguides into an octagonal cross section. We will describe in detail the fabrication of the waveguides together with their optical characterization.

In particular, the thesis is structured as follows: In Chapter 1, we present some fundamental concepts of OAM and quantum optics. In chapter 2, we present the femtosecond laser micromachining technique. We present the experimental set-up and the techniques used for device characterization in Chapter 3. The optimization and characterization of the fundamental optical components for the integrated device are presented in Chapter 4. Finally, we provide the device characterization and final design in Chapter 5.

1 Orbital Angular Momentum for Quantum Information

In this chapter, the orbital angular momentum and quantum information with OAM are briefly discussed. First, we introduce the concept of the electromagnetic field. Then the light carries the orbital angular momentum of the Laguerre-Gauss beam. The second quantization of light with the creation and annihilation operators of the photons further gives a glimpse of quantum photonics and the main building blocks. Finally, we present the role of the higher dimensional degrees of freedom in quantum information with a focus on OAM.

1.1. Maxwell's Equations and Electromagnetic Waves

One of the great discoveries that scientists made during the second half of the nineteenth century, which was developed by the English mathematician Maxwell, was that light could be described in terms of electromagnetic waves. In this section, we highlight Maxwell's theory and a few results that follow.

The equations that describe the combination of the electric and magnetic field and the response of a medium are summarized in these sets of equations [1]:

$$\nabla \cdot \vec{D} = \rho \quad (1.1)$$

$$\nabla \cdot \vec{B} = 0 \quad (1.2)$$

$$\nabla \times \vec{E} = -\frac{\partial \vec{B}}{\partial t} \quad (1.3)$$

$$\nabla \times \vec{H} = \vec{j} + \frac{\partial \vec{D}}{\partial t} \quad (1.4)$$

Where ρ is the free charge density, \vec{j} is the free current density, and \vec{B} , \vec{E} , \vec{D} and \vec{H} are the magnetic field, electric field, electric displacement, and the magnetic field respectively. In which the electric displacement has the medium response:

$$\vec{D} = \epsilon_r \epsilon_0 \vec{E} \quad (1.5)$$

$$\vec{B} = \mu_r \mu_0 \vec{H} \quad (1.6)$$

Where ϵ_r , ϵ_0 , μ_r , and μ_0 are the relative dielectric constant of a medium, dielectric constant of the vacuum, magnetic permeability of a medium, and the magnetic permeability of the vacuum.

By further assuming the medium is not magnetic $\mu_r = 1$, and it is isotropic we treat the relative dielectric constant as scalar quantity.

1.1.1. Electromagnetic Field

The electromagnetic waves propagating in linear, isotropic, free charge ($\rho = 0$), and current densities medium.

$$\vec{j} = 0, \quad \rho = 0 \quad (1.7)$$

We take the curl of the eq (2.3):

$$\nabla \times \nabla \times \vec{E} = -\frac{\partial (\nabla \times \vec{B})}{\partial t} \quad (1.8)$$

We can write it in a more compact way:

$$\nabla \times \nabla \times \vec{E} = \nabla(\nabla \cdot \vec{E}) - \nabla^2 \vec{E} \quad (1.9)$$

From the previous assumption of the free charge and the isotropic medium, where the relative dielectric constant does not change over the medium, and eq (1.1) and eq (1.5):

$$\nabla \cdot \vec{D} = \nabla \cdot \epsilon_0 \epsilon_r \vec{E} = 0 \quad (1.10)$$

Obtaining the propagation equation in a medium with certain characteristic.

$$\nabla^2 \vec{E} = \mu_0 \epsilon_0 \epsilon_r \frac{\partial^2 \vec{E}}{\partial t^2} \quad (1.11)$$

Where the Laplacian of the cartesian coordinates written as:

$$\nabla^2 = \frac{\partial^2}{\partial x^2} + \frac{\partial^2}{\partial y^2} + \frac{\partial^2}{\partial z^2} \quad (1.12)$$

The eq (1.6) describes the electromagnetic waves with a speed v given by the following expression inside the medium:

$$v = \frac{1}{\sqrt{\mu_0 \epsilon_0 \epsilon_r}} = \frac{c}{n} \quad (1.13)$$

And

$$\vec{k} = \frac{c}{n} \omega \quad (1.14)$$

Where $n = \sqrt{\epsilon_r}$ represents the refractive index of the medium, then the propagation equation is written in a form of Helmholtz equation of electric field:

$$(\nabla^2 + \vec{k}^2)\vec{E} = 0 \quad (1.15)$$

The same expression can be derived for the magnetic field \vec{H} as well.

The generic solution of the eq (1.6) is a plan wave that has an angular frequency ω and a wave vector \vec{k} of the propagating field.

$$\vec{E}(\vec{r}, t) = E_0 \exp\left(i(\vec{k}\vec{r} - \omega t)\right) \quad (1.16)$$

Where E_0 is the amplitude of the field in the cartesian coordinate, In the next section, we will introduce the concept of waveguides as guiding structures of light.

1.1.2. The polarization

The polarization of the electromagnetic waves is defined as the direction of the electric field. There are several forms of the polarization.

Linear polarization: the electric field vector points along a constant direction that may be used. Being a transverse wave, the electric field contains only components in x and y directions, having the same phase of between the two components. By considering the electric field that is linearly polarized with polarization vector \vec{u}_y or \vec{u}_x , and propagates along z:

$$E = E_y(x, z)\vec{u}_y \quad E = E_x(y, z)\vec{u}_x \quad E_z = 0 \quad (1.17)$$

At this stage, we can write the full mathematical description of a phase difference between waves of different linear polarizations as follows:

$$E(z, t) = (E_y\vec{u}_y + E_x\vec{u}_x) e^{i(k_z z - \omega t)} \quad (1.18)$$

Circular polarization: the two components of the electric field have identical amplitude but differ in phase by 90° , and the field can be described as follows:

$$E(z, t) = E_0(\vec{u}_y \pm i\vec{u}_x) e^{i(k_z z - \omega t)} \quad (1.19)$$

The field vector rotates during the propagation of the field. Either the light rotates in the plane of the propagation in clockwise direction, called right circularly polarized, or in counterclockwise direction, called left circularly polarized.

Elliptical polarization: the amplitudes of the electric field component along x and y have different magnitudes but a same phase. If the phase between the amplitudes is $E_x/E_y = r e^{i\alpha}$, the electric field vector E has its axes rotated by an angle $\alpha/2$, and if $r = 1$, we go back to the linear polarization.

1.1.3. Waveguide Structure

We will discuss the so-called slab waveguide as an introduction to guided optics. With the term slab waveguide, we usually refer to a planar and step-index waveguide, that is solved analytically. Moreover, it is a prototype of a complex guiding structure.

The slab waveguide constitutes three different regions; an inner region with a refractive index n_1 called the core; and two outer regions with a refractive index n_2, n_3 called the cladding, to have a guiding medium. To obtain the classical picture of total internal refraction (light confinement), the following conditions must be met:

$$n_1 > n_0, \quad n_2, n_3 = n_0$$

The wave propagates inside the confining region along z direction can be described using the equation (1.17). Assuming the light is linearly polarized and the propagating medium is not birefringent, we can use the scalar wave approximation, then the electric field could be presented in scalar form as follows:

$$\vec{E} = E_0(x)e^{i(\beta z - \omega t)}\vec{u}_y \quad (1.20)$$

Where β is the propagation constant, from now on we can recall the propagation equation in scalar form that has variables with scalar quantities as follows:

$$\nabla^2 E = \mu_0 \epsilon_0 \epsilon_r \frac{\partial^2 E}{\partial t^2} \quad (1.21)$$

Where the Laplacian is:

$$\nabla^2 E = \left(\frac{\partial^2 E_0}{\partial x^2} e^{i(\beta z - \omega t)} + \beta^2 E_0 e^{i(\beta z - \omega t)} \right) \vec{u}_y \quad (1.22)$$

And the right-hand side:

$$\mu_0 \epsilon_0 \epsilon_r \frac{\partial^2 E}{\partial t^2} = -k_0^2 n^2 E_0 e^{i(\beta z - \omega t)} \vec{u}_y \quad (1.23)$$

Finally, we get the eigenvalue equation. Its solutions are the eigenfunctions of the transversal profile of the electric field, whose eigenvalues are the propagation constant.

$$\frac{\partial^2 E_0}{\partial x^2} + (k_0^2 n^2 - \beta^2) E_0 = 0 \quad (1.24)$$

This is analogous to the Schrodinger equation of a particle confined in a potential well.

$$\frac{\hbar^2}{2m} \frac{\partial^2 \psi}{\partial x^2} + (\mathcal{E} - V(x)) \psi = 0 \quad (1.25)$$

Where ψ is the wavefunction associated with the particle, $V(x)$ is the potential, and \mathcal{E} is the energy. The difference between the energy and the potential is identical to the difference between the wave number times the refractive and the propagation constant. Solving the equation (1.15) leads us to certain number of different propagation constants to which we associate to different transversal profiles. To have confinement of the mode, we need to have a refractive index in the core n_1 higher than the refractive index in the claddings n_0 , and in case of particle the potential well, the potential in the well V_1 is lower than the potential of the barrier V_0 :

$$n_1 > n_0, \quad V_1 < V_0$$

We can deduce by doing further analytical derivation of the field in the transversal coordinate x of the waveguide, where the EM field decays exponentially at the boundaries with the cladding, and it will be sinusoidal at the core region [76].

1.1.4. Gaussian Beam

A wavefunction of the electric field that propagates in one direction and very slowly in the other two axes is used to describe a gaussian beam. As a result, it exhibits both plane wave and spherical wave properties. Let's choose z as the beam axis of propagation. The amplitude of the beam will reduce as z increases. Additionally, when x and y increase, the amplitude rapidly decreases.

The paraxial approximation imposes the complex amplitude of the field as follows:

$$E(x, y, z, t) \rightarrow E(x, y, z) \exp(i(kz - \omega t)) = \psi(r) \quad (1.26)$$

The solution of the Helmholtz equation (eq 2.10) that we derived in a vacuum under the paraxial approximation leads to the following:

$$\frac{\partial^2 E}{\partial x^2} + \frac{\partial^2 E}{\partial y^2} + \frac{\partial^2 u}{\partial z^2} + 2ik \frac{\partial E}{\partial z} = 0 \quad (1.27)$$

Since the laser beam diverges slowly during the propagation, we adopt the Slowly Varying Approximation (SVA) where $\frac{\partial^2 E}{\partial z^2} \ll ik \frac{\partial E}{\partial z}$. As a result, the paraxial wave equation could be written as follows:

$$\frac{\partial^2 E}{\partial x^2} + \frac{\partial^2 E}{\partial y^2} + 2ik \frac{\partial E}{\partial z} = 0 \quad (1.28)$$

The zeroth order solutions are written in the following form:

$$E(x, y, z) = E_0 \frac{w_0}{w(z)} \exp\left(\frac{(x^2 + y^2)}{w(z)^2}\right) \cdot \exp\left(-i\left(k_z z + k_0 \frac{(x^2 + y^2)}{2R(z)} - g(z)\right)\right) \quad (1.29)$$

Where $R(z), w(z) = w_0 \sqrt{1 + \frac{z^2}{(\frac{\pi w_0^2}{\lambda})^2}}$, and $g(z)$ are the radius of the beam, the beam waist, and the Gouy phase, respectively [4].

1.1.5. Laguerre-Gauss mode (LG)

The Laguerre-Gauss mode, which is the solution of the paraxial wave equation in the cylindrical coordinates, Where the complex amplitude of the LG mode will be as follows:

$$E(s, \varphi, z) = E_0 \frac{w_0}{w(z)} \left(\frac{s\sqrt{2}}{w(z)}\right)^l L_P^l \left(\frac{2s^2}{w^2(z)}\right) e^{\left(\frac{s^2}{w(z)^2}\right)} e^{-\frac{ik_0 s^2 z}{2(z^2 + z_R^2)}} e^{il\varphi} e^{ig(z)} \quad (1.30)$$

The L_P^l is the Laguerre polynomial, and the rest are similar to what we indicated recently. The phase $e^{il\varphi}$ represents the field dependance on the azimuthal angle, with an integer l .

The Laguerre-Gauss beam is generated via several ways in which the Gaussian beam wavefront obtains a helical phase and the projected beam acquires a doughnut shape (central singularity) in the radial coordinates. The presence of this central singularity is due to the destructive interference of the field. Furthermore, we will go over how these modes could be generated later [4].

1.2. Quantization of The Electromagnetic Field

The quantization of the electromagnetic field is crucial method to understand the quantum nature of the light. The fully quantum approach theory developed starting from an equivalent quantum harmonic oscillator. The theory treats the light as an individual particle.

We begin with a confined field in one dimensional cavity that has perfectly conducting walls at z , where the field is vanishing at the boundaries. We have an electric field that is function of

position and time in Fourier component of modes, decomposing it in the cavity. The cavity has a volume V and contains an infinite number of modes that have k wave numbers and frequencies ω_k [1]:

$$\vec{E}(r, t) = i \sum_k \sqrt{\frac{\hbar\omega}{2\varepsilon_0 V}} \vec{e}_k \left[A_k e^{i(\vec{k}r + \omega t)} + cc \right] \quad (1.31)$$

Where the \vec{e}_k is a unit vector of the polarization, and A_k is the amplitude of the electric field. The classical Hamiltonian of the single mode field is written as follows:

$$H = \frac{1}{2} \int dV \left[\varepsilon_0 E^2(r, t) + \frac{1}{\mu_0} B^2(r, t) \right] \quad (1.32)$$

We can introduce the two conjugate variables $q_{\vec{k}}$ and $p_{\vec{k}}$ such that:

$$A_k(t) = \frac{1}{2\omega\sqrt{\varepsilon_0 V}} (\omega q_k + ip_k) \quad (1.33)$$

$$A_k^*(t) = \frac{1}{2\omega\sqrt{\varepsilon_0 V}} (\omega q_k - ip_k) \quad (1.34)$$

The two conjugated variables satisfy the Hamilton equations:

$$\dot{q}_k = \frac{\partial H_k}{\partial p_k} \quad \dot{p}_k = -\frac{\partial H_k}{\partial q_k} \quad (1.35)$$

We can thus rewrite the Hamiltonian in terms of these two operators as:

$$H = \frac{1}{2} \sum_k (\omega^2 q_k^2 + p_k^2) \quad (1.36)$$

This equation is formally analog with the one that describing the harmonic oscillator with position and momentum variables. Thus, to quantize the field we suppose to substitute the q and p with their corresponding quantum operators, those corresponding to observable quantities which satisfy the commutation relation:

$$[\hat{q}_k, \hat{p}_k] = i\hbar\delta_{kk} \quad (1.37)$$

Furthermore, the annihilation and the creation operators are defined as a function of the previous operators as follows:

$$\hat{a} = \frac{1}{\sqrt{2\hbar\omega}}(\omega\hat{q} + i\hat{p}) \quad (1.38)$$

$$\hat{a}^\dagger = \frac{1}{\sqrt{2\hbar\omega}}(\omega\hat{q} - i\hat{p}) \quad (1.39)$$

This leads as to write the Hamilton in more compact way as follows:

$$\hat{H} = \hbar\omega\left(\hat{a}^\dagger\hat{a} + \frac{1}{2}\right) \quad (1.40)$$

The number operator could be defined as $\hat{n} = \hat{a}^\dagger\hat{a}$ whose eigenstate is the photon number state.

$$\hat{a}^\dagger\hat{a}|n\rangle = \hat{n}|n\rangle = n|n\rangle \quad (1.41)$$

So, the energy of the system is given in terms of the number operator, which attributes to each photon of energy $\hbar\omega$. Notice that having an energy when there are no photons, which correspond to the energy of the vacuum [1].

$$\hat{H}|n\rangle = \hbar\omega\left(\hat{n} + \frac{1}{2}\right)|n\rangle = E_n|n\rangle \quad (1.42)$$

1.3. The Angular Momentum

Based on the observation that comet tails usually pointed away from the sun, Kepler postulated that light must have a linear motion as early as the 1600s. Maxwell's equations contain all of the momentum and energy characteristics of light, but Poynting did explain that a circularly polarized light beam possessed an angular momentum that we would today assign to the spin of individual photons until 1909, where because every polarization vector rotates around itself (Fig 1.2) [14]. Darwin noted that in addition to this spin angular momentum, higher order atomic/molecular transitions require an optical angular momentum of several units per photon to maintain angular momentum. This additional angular momentum is called "orbital angular momentum OAM" and it results from light's linear momentum operating off-axis with regard

to the optical beam's center in different meaning the wavefront of the light rotates around the propagation axes (Fig. 1.1) or the center of mass of the interacting object [13].

In 1992, Allen and his co-works demonstrated that light beams with helical phase-fronts are defined by a transverse phase structure of $e^{il\phi}$, and each photon has an orbital angular momentum equal to $l\hbar$. An important characteristic of a beam that has helical phase is the singularity, where OAM-carrying beams often have annular intensity cross-sections because the phase singularity causes the optical intensity to be exactly zero in the center [15].

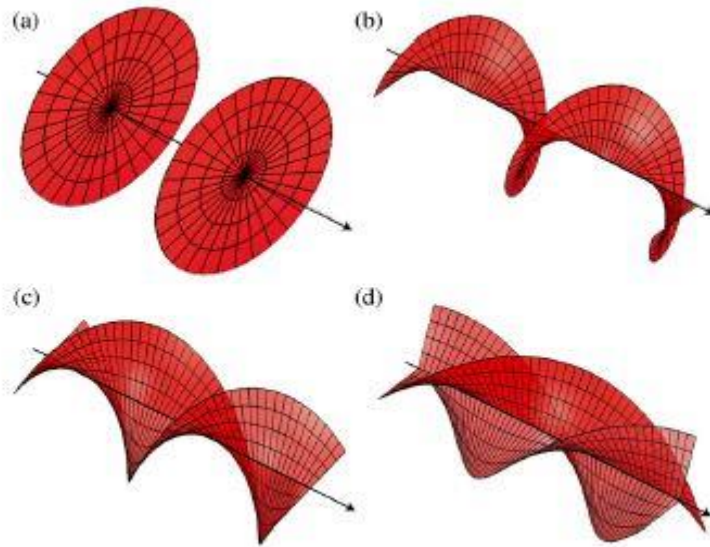


Figure 1.1: Shaped helical phase front of OAM (a) $l = 0$, (b) $l = 1$, (c) $l = 2$, (d) $l = 3$

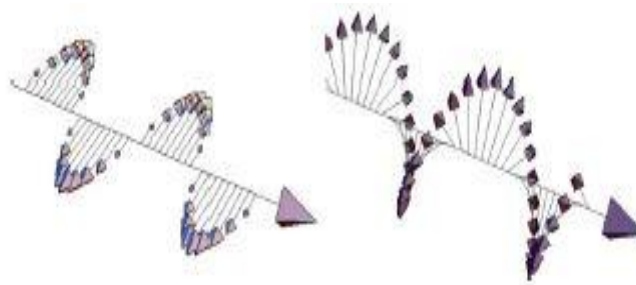


Figure 1.2: Spin Angular Momentum connected to the polarized field. Light has a linear polarization (left) have no SAM, the circularly polarized field (right) carries SAM.

1.4. Orbital Angular Momentum of Light

The link that Allen et al. make between beams with helical phase-fronts and orbital angular momentum lies at the heart of their study. These helically phased beams, however, have already been created and analyzed in the past, not least as illustrations of the transverse modes formed from appropriately designed laser cavities or as a result of optical vortices [16]. Since the 1970s,

there has also been a great deal of research done on optical vortices that include phase singularities [17]. However, no work had been done in any of these prior research between these characteristics and the angular momentum in the beam. Many techniques have been exploited to generate the beams that have OAM. We can further discuss the conventional methods of the bulk optics components that are commonly used. In addition, the very recent technology of integrated photonics circuits is exploited to generate light beams that carry OAM.

Cylindrical Lenses

The first technique for creating OAM was the Cylindrical Lenses, where It involves employing two cylindrical lenses to convert Gaussian beam that emitted by a laser into a helically phased Laguerre-Gaussian mode (LG). To generate an LG mode, each sequence of the gaussian modes goes through a series of phase plates with a thickness that increased with azimuthal angle, such that the projected beam acquires a transvers phase of $e^{il\varphi}$ [13].

Diffraction Gratings and Spatial Light Modulators (SLM)

The diffraction grating with l -pronked fork dislocation in the ruled to lines is employed to produce helically-phased beams. According to research by Soskin and colleagues, a plane-waved incident beam that is aligned coaxially with this dislocation produces a first-order diffracted beam with helical phase-fronts that are once more characterized by $e^{il\varphi}$. The commercial availability of computer addressable, pixelated, spatial light modulators that can be configured to function as reconfigurable diffractive optical components makes this diffractive-optic technique much more applicable. Additionally, a variety of algorithms are available for SLM device aberration correction, resulting in excellent optical fidelity beams. The majority of SLMs used for OAM research are built on thin liquid crystal films whose refractive index can be switched locally by applying an electric field. If the films are placed over a pixelated electronic array, this property can be controlled to give the reflected light a spatially dependent phase variation [18].

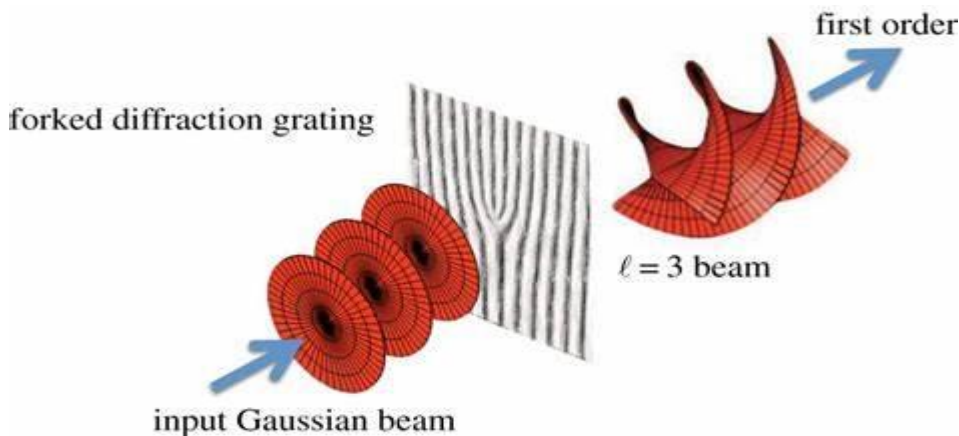


Figure 1.3: Spatial light modulator surface used to reshape the Gaussian beam to a beam carrying OAM with helical phase and integer $l = 3$.

Ring Resonator

The light with orbital angular momentum is generated via a ring resonator with a group of nano-rods around it. The nano-rods scatter the evanescent waves of the circulating light in the ring, which creates a rotating electromagnetic field with only angular momentum and no linear momentum along the rotation axis. The difference between the number of rods and the order of the Whispering Gallery mode determines the angular integer, and the light frequency divided by the angular order determines the rotational frequency [19].

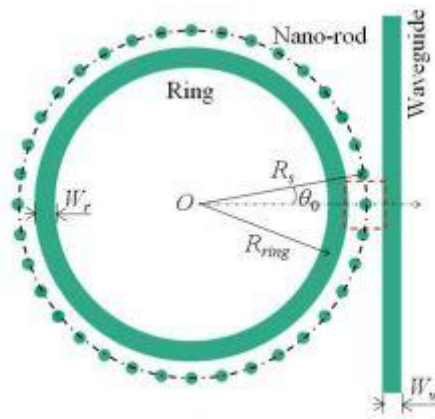


Figure 1.4: Ring resonator surrounded by group of nano-rods to emit the light that carrying OAM [19].

Single Mode Waveguides

Generating OAM with the bulk optics requires specific and precise alignment of the optical setup. The single mode waveguide (SMW) that was fabricated via femtosecond laser technology could solve most of the problems, such as the difficulties of the setup, miniaturization, and stability. A recent proposal by Crespi *et al* involves the properties of the projected beam from a set of SMW distributed over polygonal cross-section. The output of the engineered SMW is approximated as a gaussian mode, in which the properties of the projected beams in the far field form beams carrying OAM. The zero field in the middle (singularity) is due to the destructive interference (Figure 1.5). The helical phase is applied using a phase thermal shifters that enable us to control the OAM integer $\pm l$ [3]. It is shown that a hybrid photonic integrated circuit that multiplexes and demultiplexes 15 OAM states is made up of three-dimensional femtosecond laser-written waveguide. For the purpose of confirming that the hybrid OAM produced the right azimuthal phase for each of the 15 OAM states, spatial shearing interferometry enabled near-field phase characterization. The average device crosstalk in a retro-reflection multiplexing/demultiplexing setup was 17 dB, while the highest crosstalk was 8 dB [20]. LG modes have recently gained interest in a variety of applications ranging from free space to fiber communication based for both classical and quantum applications, as we will discuss later.

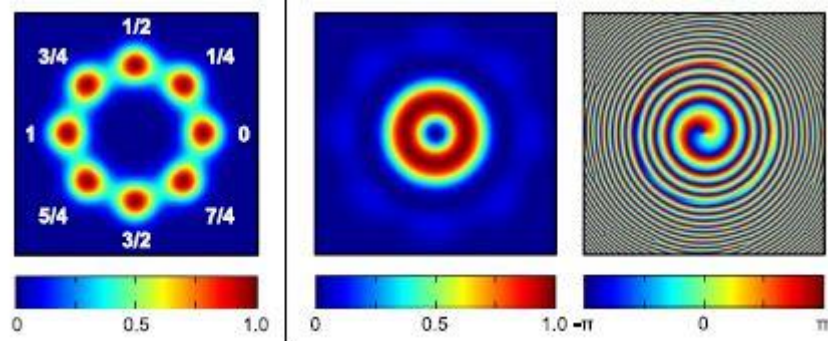


Figure 1.5: Simulation of SMW of 8 waveguides in a vertices of octagonal lattice. (Left panel) near field projection. (Middle panel) far field distribution that shows Laguerre-Gauss mode with singularity and integer $l = 1$. (Right panel) A helical phase [3].

1.5. Ring Core Optical Fiber

The ability to deliver light beams with OAM without a loss of information can be performed using a special kind of fiber with a ring-shaped core. Indeed, optical fiber-based communications can be the best choice to have an efficient transport

The so-called ring core fiber (RCF) consists in a cylindrical dielectric and step-index guiding structure of circular cross-section (figure 1.6). The fiber is made of a transparent material to light over the operating wavelength. The fiber structure should meet the following conditions:

$$n(r) = \begin{cases} n_1 = n_0, & a > r \\ n_2 = n', & a \leq r \leq b \\ n_3 = n_0, & b < r \end{cases} \quad (1.43)$$

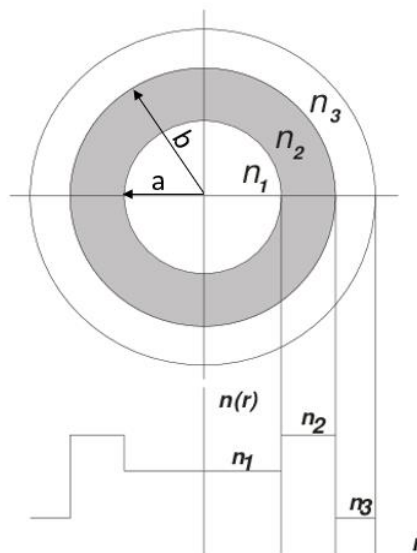


Figure 1.6: A representation of RCF, where the light propagates in annular core with internal and external radius a and b , with refractive index n_1 at the central core and n_3 at the outer region, where the annular region has the highest refractive index n_2 .

We have three different regions, the inner region is the core ($r \leq a$) with a refractive index n_0 , the annular region ($b \geq r \geq a$) has a refractive index n' that is the highest in our contrast, and the outer region ($r > b$) has a refractive index n_0 that is equal to the one of the core.

The electric field waves are described by the wave equation that we have derived in the previous chapter, under the scalar wave approximation, and the medium is assumed to be isotropic, homogeneous, and non-birefringent.

$$\nabla^2 E = \frac{1}{v^2} \frac{\partial^2 E}{\partial t^2} \quad (1.44)$$

It is convenient due to the cylindrical symmetry to adopt the cylindrical coordinates (r, φ, z) :

$$\nabla^2 E = \frac{\partial^2 E}{\partial r^2} + \frac{1}{r} \frac{\partial E}{\partial r} + \frac{1}{r^2} \frac{\partial^2 E}{\partial \varphi^2} + \frac{\partial^2 E}{\partial z^2} \quad (1.45)$$

Symmetry requires the field to have a dependence on the azimuthal angle φ that is expressed as $e^{-il\varphi}$. Overall, the electric field in optical fibers is expressed in the cylindrical coordinates as:

$$E(r, \varphi, z, t) = E_r e^{-i\beta z} e^{-il\varphi} e^{i\omega t} \quad (1.46)$$

The β is the propagation constant of the light that propagates along the z direction, l is an integer represents the order of the OAM, and ω is the angular frequency of the field. The $E_r = E_r(r)$ only depends on the radial coordinate.

$$\frac{\partial^2}{\partial z^2} e^{-i\beta z} = -\beta^2 e^{-i\beta z}, \quad \frac{n_r}{c^2} \frac{\partial^2}{\partial t^2} e^{i\omega t} = n_r k_0^2 e^{i\omega t}, \quad \frac{1}{r^2} \frac{\partial^2}{\partial \varphi^2} e^{-il\varphi} = \frac{-l^2}{r^2} e^{-il\varphi}$$

The solutions of the propagation equations in the three regions satisfy the following equation:

$$\frac{\partial^2 E_r}{\partial r^2} + \frac{1}{r} \frac{\partial E_r}{\partial r} + \left[k^2 n_r^2 - \beta^2 - \frac{l^2}{r^2} \right] E_r = 0 \quad (1.47)$$

This is actually, an eigenvalue equation, whose solutions are the eigenfunctions of the transversal amplitude profile of the electric field, and whose eigenvalues are the propagation constants β . More precisely, we can rewrite Eq (2.16) in the three different regions follows.

$$\begin{aligned} \frac{\partial^2 E_1}{\partial r^2} + \frac{1}{r} \frac{\partial E_1}{\partial r} - \left[\beta^2 + \frac{l^2}{r^2} - k_0^2 n_0^2 \right] E_1 &= 0 \\ \frac{\partial^2 E_2}{\partial r^2} + \frac{1}{r} \frac{\partial E_2}{\partial r} + \left[k_0^2 n_0'^2 - \beta^2 - \frac{l^2}{r^2} \right] E_2 &= 0 \\ \frac{\partial^2 E_3}{\partial r^2} + \frac{1}{r} \frac{\partial E_3}{\partial r} - \left[\beta^2 + \frac{l^2}{r^2} - k_0^2 n_0^2 \right] E_3 &= 0 \end{aligned} \quad (1.48)$$

If we define:

$$\begin{aligned} \gamma &= \sqrt{\beta^2 + \frac{l^2}{r^2} - k_0^2 n_0^2} \\ K &= \sqrt{k_0^2 n_0'^2 - \beta^2 - \frac{l^2}{r^2}} \end{aligned} \quad (1.49)$$

$$\sigma = \sqrt{\beta^2 + \frac{l^2}{r^2} - k_0^2 n_0^2}$$

We can write the wave equation as follows:

$$\frac{\partial^2 E_1}{\partial r^2} + \frac{1}{r} \frac{\partial E_1}{\partial r} - \gamma^2 E_1 = 0 \quad (1.50a)$$

$$\frac{\partial^2 E_2}{\partial r^2} + \frac{1}{r} \frac{\partial E_2}{\partial r} + K^2 E_2 = 0 \quad (1.50b)$$

$$\frac{\partial^2 E_3}{\partial r^2} + \frac{1}{r} \frac{\partial E_3}{\partial r} - \sigma^2 E_3 = 0 \quad (1.50c)$$

The solution of the equation (1.50b) is the Bessel function $J_l(Kr)$, which is the proper solution to the region (2) of the refractive index n' . The field diverges when the l order increases at $r = 0$ (figure 1.7). The proper solution of the equation (1.50a) is the modified Bessel function of the first kind $I_l(\gamma r)$, and for the equation (1.50c), the solution is the modified Bessel function of the second kind $\mathcal{K}_l(\sigma r)$. Therefore, the electric is given by:

$$E_z = \begin{cases} B_1 I_l(\gamma r) \exp(i(l\phi + \omega t - \beta z)) & 0 \leq r < a \\ A_2 J_l(kr) \exp(i(l\phi + \omega t - \beta z)) & a \leq r \leq b \\ A_3 \mathcal{K}_l(\sigma r) \exp(i(l\phi + \omega t - \beta z)) & b < r \end{cases} \quad (1.51)$$

The $A_2, B_1,$ and A_3 are multiplication coefficients.

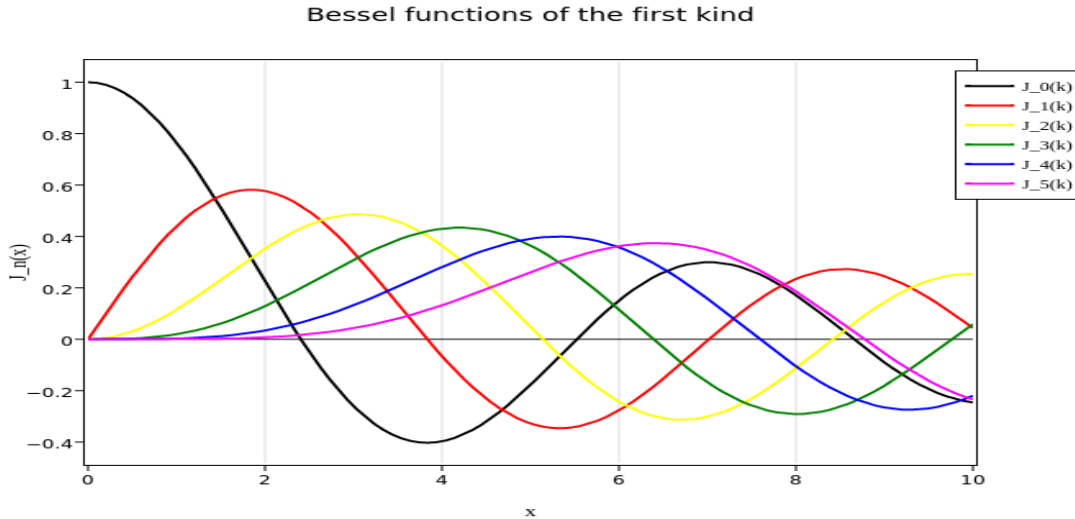


Figure 1.7: The Bessel function of order of l as a function of the transverse direction r that describes the field at the ring region of refractive index n' .

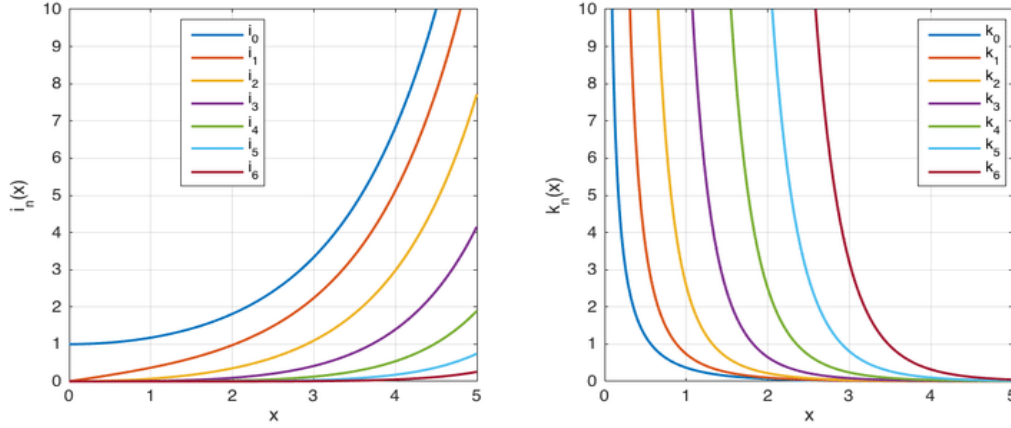


Figure (1.8): (left) first kind of the modified Bessel function of order of l as a function of the transverse direction r describes the field at the core region of refractive index n_0 . (right) that the field in the outer region of refractive index n_0 described by the second kind of the modified Bessel function.

From the solution of the Equations (1.51), we can conclude that the RCF is reliable transport of the light that carries OAM.

Using the LG beams to couple orbital angular momentum into ring core fiber has been successfully proven, but coupling several OAM is still challenging, because the diameter of the Laguerre-Gauss mode changes proportionally with respect to the integer \sqrt{l} . One would indeed need to optimize the coupling of different free space modes for each integer, which leads to a trade-off in terms of the coupling efficiency. For instance, a mode overlap of 0.95 is achieved for LG modes with $l = 4, 5$, and 6 for a ratio between the beam and the core radius of w/a , which shows higher and more homogeneous coupling efficiency, but for the lower l the overlap is less than 70% (figure 1.9a) [36].

PV Beams

A possible solution was proposed by Rojasrojas *et al*, who considered the use of the perfect vertex (PV) [36]. The PV beams are the result of the Fourier transformation of Bessel-Gaussian beams [35]. The transverse field distribution could be described as follows:

$$PV_l \approx i^{l-1} \frac{w_g}{w_0} \exp(il\varphi) \exp\left(-\frac{(r-r_r)^2}{w_0^2}\right) \quad (1.52)$$

w_0 is the beam width at the focus plane ($w_0 = 2f / kw_g$), w_g is the beam width of the Gaussian beam used to confine the Bessel beam, and $2w_0$ and r_r are the widths of the annular PV beam profiles, respectively. It is therefore feasible to tune the field amplitude to have the required transverse "ring" profile that is independent of the value of l , provided r_r is big enough for the approximation of Eq. (1.52) to be valid. PV modes have been produced using a variety of techniques, including holograms with periodic azimuthal variation, phase masks created by combining the axicon and spiral phase functions, and passive components like axicons, which have all been successfully reported [37][38][39].

We point out that OAM mode propagation through specially constructed ring core and air core fibers, which can support up to 36 and 10 OAM modes, respectively, has also been shown using

PV beams. In contrast to typical few- and multi-mode fibers, the radial profile of the LP modes varies very little with l in the RCF because the spatial modes are contained within the annular core. The PV shows, in the case of coupling efficiency, an average overlap with the RCF bound modes of 0.995 (Figure 1.9b).

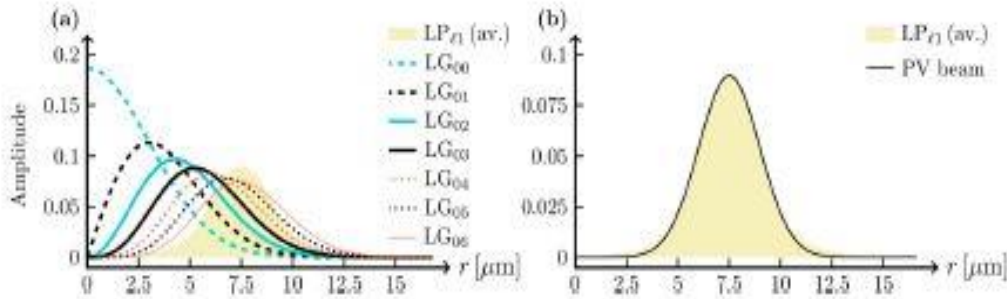


Figure 1.9: (a) The transverse profile of the LG_{0l} modes as the integer l increases with a fixed beam width. Their radius is proportional to \sqrt{l} , where the maximum overlap with the spatial mode LP that generated by the RCF achieved at $l = 6$. (b) the PV beam amplitude and the averaged amplitude of the PL modes [36].

1.6. Quantum Photonics

Information in a generic way is stored in traditional computers as binary bits, which might have a logical value of 0 or 1. Quantum computers, also known as qubits, store information similarly to their classical counterparts. These are individual particle quantum-mechanical states, such as those of atoms, photons, or nuclei. The main distinction between classical and quantum bits is that quantum bits (qubits) may take on superposition states, in which the system is simultaneously in the 0 and 1 states. This is a result of the quantum physics superposition principle, in contrast to classical systems, which can only ever be in one of the two conceivable states at a given time.

The quantum-mechanical wave function ψ controls the qubits characteristics. We define a physical system such as the polarization with horizontal and vertical polarizations that can be represented by two quantum states.

$$|\psi\rangle = c_1|H\rangle + c_2|V\rangle \quad (1.53)$$

Where the normalization condition on $|\psi\rangle$ requires that:

$$|c_1|^2 + |c_2|^2 = 1 \quad (1.54)$$

demonstrates that the system is simultaneously in H and V states in a superposition. The amplitude coefficients c_0 and c_1 control how many of each binary state there are in relation to one another [1].

There are significantly many platforms where quantum information can be encoded in a variety of physical systems such as photons, nuclear, and atomic systems.

Light is often considered the best carrier of the information as it travels with the speed of light, it has low noise interactions (do not interact with the environment), and it could be sufficiently transported via the fibers.

The quantum photonics technology requires in general three main blocks: quantum light sources, a manipulating stage (Quantum processor), and finally the quantum detectors. These blocks are extremely important to have such technology in our markets, they probably heading toward the future success parallelly [6].

Quantum Light Source

Quantum information may be sent and encoded using photons. Since each photon is equivalent to a qubit, and qubits must all be independent. Furthermore, to involve the light in the quantum experiments that requires us to have sets of indistinguishable single photons that are generated in reproducible and stable fashion, where the individual photons must be identical to each other.

The indistinguishability could be verified using Hong-Ou-Mandel experiment (Figure 1.10). The two upper mirrors' positions may be changed to adjust the delay between photons 1 and 2. We can label the photons thanks to the delay; depending on when they arrive at the detector, we can tell whether they are photons 1 or 2 [1].

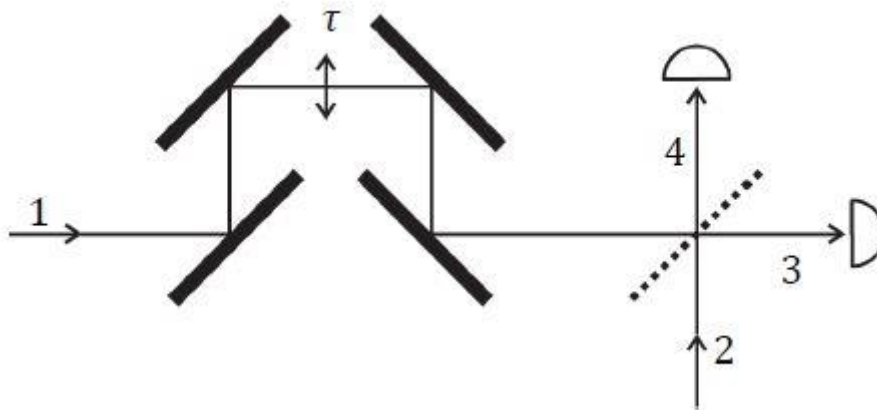


Figure 1.10: Hong-Ou-Mandel interferometer. It consists of a delay line made of four mirrors, 50:50 beam splitter, and two detectors.

There are many techniques to build single photon sources such as weak coherent pulses, spontaneous parametric down conversion (SPDC), and spontaneous four-wave mixing in optical waveguides (SPDC). These SPSs have been demonstrated in X3 waveguides (SiO₂, and Si₃N₄) [21,22], and X2 waveguides (GaAs, and LN) [23]. Integrated parametric SPSs are famous for their ability to be manufactured very similar and in an array while yet allowing for individual control of each.

Having the photon as a base for the quantum application provides us several degrees of freedom, these includes the polarization which is a two-level quantum system (horizontal and vertical

polarization). Generation and manipulation the polarization states is relatively easy with the standard bulk-optics components (Waveplates, and polarizers), were they are commonly used for quantum information encoding [5].

Integrated Photonics Devices

The second stage represents the core of the quantum photonic platform where the quantum states of light are manipulated.

Integrated photonic circuits (IPC) are considered the best choice for manipulating photonic qubits, because they allow to eliminate obstacles such a size and stability issues. The IPC are built upon architectures of directional couplers, with additional geometries to account for deformation induced. Additionally, recent advancements have demonstrated the capacity to incorporate active reconfigurable parts, enabling the creation of devices that serve many purposes. Due to its many advantages, including low propagation losses, low birefringence, functioning from the visible to the infrared spectrum, strong coupling efficiency with single mode fibers, and low temperature dependency, fused silica is still one of the most frequently utilized materials for integration. However, unlike miniature electronic circuits, linear optical circuits have several platforms or manufacturing methods [5]:

Silicon-on-Insulator

The development of Si-based platforms, such as silicon (Si), silicon nitride (SiN), and silicon carbide (SiC), derives from the know-how provided by electronic technologies. Si-based devices have an extremely high refractive index, enabling smaller circuit sizes and making them appropriate for nonlinear processes [24]. Low mode-matching with optical fibers and rather large propagation losses are limitations. Devices based on III-V compound semiconductors, such as indium phosphide, gallium arsenide, and gallium nitride, can operate under slightly better conditions.

Silicon-on-Silicon (SoS)

Waveguides with rectangular cross sections are etched onto a layer of silica (SiO₂) that is placed over a crystal silicon substrate. The doped silica core is subsequently covered by a second layer of undoped silica, which also serves to shield the waveguides [25]. Due to the birefringence caused by the rectangular cross-sections, the SoS approach is constrained by the requirement for a mask and the constraint to one polarization.

Ultraviolet Writing

By concentrating a powerful laser pulse in a photosensitive B- and Ge-doped silica layer that is sandwiched between two layers of un-doped silica and on top of a third translating silicon layer, waveguides may be inscribed [26]. This method reduces the complexity of manufacturing because it does not require masks.

Femtosecond Laser Micromachining

The process is driven by the non-linear absorption of powerful, tightly concentrated ultrashort laser pulses in a glass substrate, which results in a permanent, localized change in the refractive index. Inscribing waveguides involves translating the sample across 3D geometries with controlled speed [27].

Silica's low birefringence and the ability to write circular cross-sections make it possible to create waveguides that depend little on polarization. On the aforementioned platforms, photonic circuits may be built using linear-optical interferometric techniques that can carry out arbitrary unitary evolutions [28].

There have been many breakthrough achievements recently in the quantum photonic field. 12-modes quantum photonics processor that is also called universal multiport interferometers (UMI), which is a completely reconfigurable hardware controlled via the thermo-optics effect [8]. Quantum walks for simulation considered as a resource structure for quantum simulations, quantum walks are the extension of classical random walks to a quantum environment. Discrete-time quantum walks, where the evolution is stroboscopic because it happens in discrete steps, and continuous-time quantum walks, where the evolution on a given lattice is described by a Hamiltonian associated with the coupling between the various sites, can be divided into two different classes. Both the single-particle and multi-particle regimes, where quantum interference between the several particles occurs throughout the quantum dynamics, have been used to perform quantum walks [29].

The continuous-time quantum walk has been adopted to shed light on the interplay between quantum coherence and noise for assist transport processes in complex networks [33]. Molecular simulation is fundamentally important in quantum chemistry to effectively model the molecular characteristics. In IQP chips, a variational eigen-solver and quantum phase estimation were used to determine the ground-state energies of molecules like H₂ and He-H⁺. The eigenvalues for both ground and excited states were approximated using an algorithm that combined these two methods. Experimentally, both the ground and excited states are identified with fidelities >99%, and their eigenvalues are calculated with 32 bits of accuracy [30][31].

It was designed an optical memristive element that enables the transmission of coherent quantum information as a superposition of single photons on spatial modes. The first experimental demonstration of a quantum memristor realized by a prototype of such a device on a glass-based, laser-written photonic processor. Then, a designed memristor-based quantum reservoir computer was implemented and numerically tested on both classical and quantum tasks, achieving strong performance with incredibly constrained physical and computational resources and, most importantly, maintaining the same architectural design throughout [32].

Quantum Detector

photodetectors are devices that produce a macroscopic electric signal when it gets triggered by only one incoming photon or by at least one photon (photon number resolving detector PNR). Detecting photons with high probability and reliability is a key requirement for most tasks, often representing a bottleneck for the overall efficiency of an apparatus. Due to the very low energy of a single photon (10⁻¹⁹). High gain and low noise are necessary for the (PNR) detector to be able to distinguish the correct number. Non-PNR detectors such as single-photon avalanche photodiodes (SPAD) or negative feedback avalanche diodes (Si-based SPADs) work

well with visible light but struggle in the infrared window because strong IR absorption and low noise are incompatible [34].

1.7. Quantum Information and Higher Dimensional Quantum States

Modern technological advancement has been significantly affected by quantum information. The previous two decades have seen intense research activity in this area, with excellent outcomes in areas including quantum computing, communication, and simulation. The classical bit, which is a two-level quantum system and the fundamental building block of quantum information, has a quantum equivalent known as a qubit. Although these were initially demanding tasks, controlling and manipulating qubits is now common practice in quantum investigations. Exploiting d-level quantum systems, also known as qudits, makes it fascinating to study quantum information in larger Hilbert spaces [12].

A qudit is a quantum system that is not constrained into a 2D space and that, in principle, can have any integer number d of levels. The quantum-mechanical wave function ψ controls the qudits characteristics. We define a physical system such as quantum light that carrying OAM of an integer l that can be represented as follows:

$$|\psi\rangle = \sum_{l=-\infty}^{+\infty} c_l |+\!l\rangle_1 |-\!l\rangle_2 \quad (1.55)$$

where $|\pm l\rangle$ and c_l are the photon states with OAM integer $|\pm l\rangle$ and complex probability amplitudes. Experimental conditions impose boundaries on, that is, on the Hilbert space spanned, so that $l \in \{-d, \dots, d\}$.

Generation of High-dimensional Quantum States

To expand the Hilbert space, different photonic degrees of freedom or combinations of them can be used to generate qudits. In addition, the higher dimensional quantum states could be generated using bulk optics or integrated optics.

OAM

Photon pairs entangled in their orbital angular momentum can be produced using SPDC in a nonlinear crystal. Due to the conservation of OAM (when the pump photon has CP), the two photons have opposite OAM values CP such that the resulting two-photon state can be written as:

$$|\psi\rangle = c_0 |0\rangle_s |0\rangle_i + c_1 |-\!1\rangle_s |1\rangle_i + c_2 |1\rangle_s |-\!1\rangle_i + \dots = \sum_{l=-\infty}^{+\infty} c_l |+\!l\rangle_s |-\!l\rangle_i \quad (1.56)$$

The creation of states like 4D Bell states [40], quantum Greenberger-Horne-Zeilinger (GHZ) states [41], or multiphoton entanglement in high dimensions is made possible by the proper engineering of such photon sources. It is suggested to use a highly innovative method to create

OAM high-dimensional states. The experimental setup was carefully installed by the authors such that Hong-Ou-Mandel interference could be used to post-select high-dimensional entangled states [42]. The following chapter will go into more depth on the creation and transmission of OAM states across waveguides, which is a very challenging process.

Temporal Structure of Light

The time of the photon emission could be counted as a degree of freedom. The SPDC method allows for the generation of qudits, where time-energy and time-bin entangled qudits can be created in this fashion. In the first scenario, the Heisenberg uncertainty relation specifies an uncertainty Δt for the photon pair emission timings. The coherence time of the pumping laser t_p , which is inversely correlated to the corresponding linewidth in the spectral domain, may be used to explain the uncertainty Δt . As a result, extended coherence time is produced by pumping a crystal with a narrowband laser, allowing for higher uncertainty in the photon pairs' emission times and resulting in entanglement in the temporal domain. The states generated by this process can be written as:

$$|\psi\rangle = \sum_{k=1}^d a_k |k\rangle_1 |k\rangle_2 \quad (1.57)$$

where a_k is a complex probability amplitude and $|k\rangle$ denotes a photon in the k th time slot of the pump's coherence time. It is possible to measure the entangled qudits produced in this manner using unbalanced Mach-Zehnder interferometers, also referred to as Franson interferometers [43]. Numerous studies have employed time encoding, mostly with an emphasis on quantum communication and quantum cryptography [44][45].

A time-bin entangled qudit's creation is not significantly different from a time-energy one. In contrast to the former, the latter requires that the discretization into several temporal states occur within the coherence length, whilst the former does not. A pulsed pump is required to produce time-bin entangled states so that each time state may be uniquely identified by the pulse that produced the photon pair. The length of the Hilbert space covered increases with the number of pump pulses taken into account. Like previously, Franson interferometers are required in this instance or a combination of them to disclose the entanglement between the states.

Frequency

Frequency-entangled qudits can be generated starting from a parametric down-conversion process. The two-photon state from an SPDC process can be described as:

$$\int_{-\infty}^{+\infty} d_s d_i f(\omega_s, \omega_i) \hat{a}_s^\dagger(\omega_s) \hat{a}_i^\dagger(\omega_i) |0\rangle \quad (1.58)$$

with \hat{a}^\dagger being the creation operator at angular frequency ω , the subscripts s and i indicating the signal and idler photons, respectively, and $f(\omega_s, \omega_i)$ being their joint spectral amplitude, which depends on the crystal and the pumping light. A clever way to create frequency-entangled qudits is proposed in ref. [46]. The authors combined the photon pair state as described in Equation (1.58) together with the Hong–Ou–Mandel interference.

Path

The Path has been investigated as a novel way to create entanglement in higher dimensions. The authors demonstrate how route identity may produce two-photon arbitrary high-dimensional entanglement. The formation of photon pairs in various crystals and the overlapping of their trajectories, starting with separable (nonentangled) photons, results in various kinds of entanglement in high dimensions. The authors demonstrate the method's remarkable versatility by employing modes and phase-shifters to properly regulate which state is generated. Combinations of multiport beam-splitters can be constructed properly to have non-classical correlations in higher dimensions in the path, as demonstrated by Zukowski and coauthors [47].

Composition of Degrees of Freedom

Every degree of freedom considered has advantages and limitations in real life. However, combining them can occasionally make it easier to explore bigger Hilbert spaces. For instance, polarization bases may be mixed with practically all of the other degrees of freedom, even though they reside in a 2D Hilbert space. Indeed, taking into account hybrid high-dimensional situations has led to several notable and essential discoveries. Spin-orbit states (a mix of polarization and OAM), path-polarization states, polarization-time states, and frequency-path states are a few examples of hybrid qudits [48][49].

Advantages of High-Dimensional Quantum States

Qubits are the basic quantum information units and are described by a basis of two orthonormal vector states. Conversely, a qudit is a quantum system that is not constrained into a 2D space and that, in principle, can have any integer number d of levels. We are going to highlight what are the possible advantages that are offered by such high-dimensional systems.

Higher information Capacity

The enhanced information capacity per quantum system is the first and most obvious benefit provided by qudits. For instance, the following two bits of information can be encoded using high-dimensional states with $d = 4$: $|0\rangle = 00$, $|1\rangle = 01$, $|2\rangle = 10$, and $|3\rangle = 11$. The relation $\log_2 d$, which yields the number of traditional bits (or qubits) required to encode the same amount of information, provides a quantifiable measure of the increased information capacity. High-dimensional entangled states further produce a higher channel capacity, or the volume of data that may be successfully conveyed through a communication channel. Through experimentation, bipartite entangled qudit has been shown to overcome the capacity of the traditional channel [50].

Higher Noise Resilience

High-dimensional quantum states have a crucial property for quantum communication in addition to their enhanced information capacity: they are more resistant to noise, whether it comes from the outside or from eavesdropping attempts. When calculating the increased resistance to noise sources held by qudits, it is taken into account that both 2 and $d + 1$ are

used to compute the information obtained by a prospective eavesdropper during coherent attacks. It has been shown that the resilience of qudits to noise grows with their dimension d [51].

2 Femtosecond Laser Written Waveguides

In this chapter we will focus on the femtosecond laser micromachining (FLM) technique for optical devices fabrication. We also discuss how Single Mode Waveguides (SMW) are engineered in a certain scheme can generate and manipulate light beams carrying OAM, for quantum communication applications. Over the last decades, this technology has been exploited in different applications, mainly waveguide fabrication in transparent materials for integrated photonics devices [52][53].

Femtosecond laser written waveguide is based on the non-linear absorption of focused pulse in the transparent material. This leads to a smooth and permanent modification of the refractive index in corresponding of the focal spot. Comparing the FLM technique for the waveguide fabrication with the traditional methods, it shows several advantages, such as no need for the clean-room labs, possibility to define arbitrary structures of waveguide in three dimensions, fast and cost-effective prototyping of optical devices.

2.1. Femtosecond Pulse and Matter Interaction

A non-linear absorption nature induces changes to certain focal volume in bulk material is taking place, this ability to micromachine geometrically complicated objects in three dimensions is made feasible by this spatial confinement in combination with sample translation or laser-beam scanning. Second, the absorption process is material-independent, making it possible to construct optical devices on compound substrates made of various materials [54].

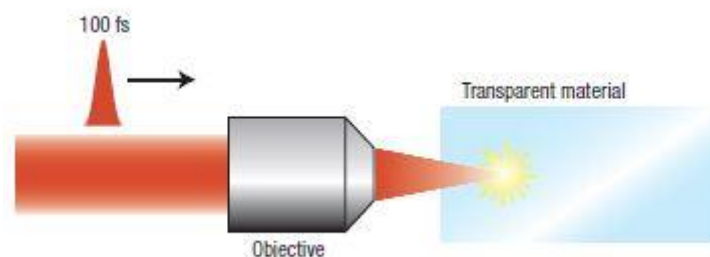


Figure 2.1: Femtosecond Laser Micromachining incident on dielectric material

2.1.1. Non-Linear Absorption

When a pulsed laser of a high peak intensity interacts with dielectric material, the energy is partially transferred to the material (electrons excitation), then the highly excited electrons

thermalize with the ions and change the material permanently. For pulses longer than 10 fs the electrons are excited via phonon-mediated linear absorption. When they gain enough kinetic energy to excite other bounded electrons, and when the density of the excited electrons arrives to about $10^{29} m^{-3}$ the electrons behave like plasma with frequency resonant to the laser, leading to the absorption of the remaining pulse energy [54]. Initial electrons excitation occurs via a non-linear phenomenon, such as multiphoton. Ionization and may continue via avalanche ionization.

If a long pulse laser used to illuminate the dielectric (with several picoseconds or nanosecond duration), the peak intensity is too low to allow multiphoton or tunneling ionization processes, even if the energy was so high. The only possible absorption mechanism is avalanche ionization.

High Intensity Regimes

Multiphoton ionization requires a simultaneous absorption of the photons, the energy of each photon is $h\nu$, typically in femtosecond laser matter interaction the multiphoton ionization is dominant such that

$$N h \nu > E_g \quad (2.1)$$

where h is plank constant, N is the integer that represents the minimum number of the photons required to exceed the energy gap of the material, ν is the frequency and E is the energy gap (energy difference between the conduction and valence band) [55].

Tunneling ionization is related to the very high electric field of the pulsed laser that leads to decreasing the Coulomb potential energy barrier, which allows the electrons to tunnel from the valence band to the conduction band [55].

Low Intensity Regimes

Avalanche ionization the free electrons at the bottom of the conduction band get accelerated due to the incident light field and acquire kinetic energy, when the total energy of the accelerated electron gets higher than the minimum level of a conduction band, it can ionize another electron from the valence band, and then results in two electrons at the minimum level of the conduction band. The two electrons could be as well accelerated by the incident field resulting the same process which causing avalanche [55].

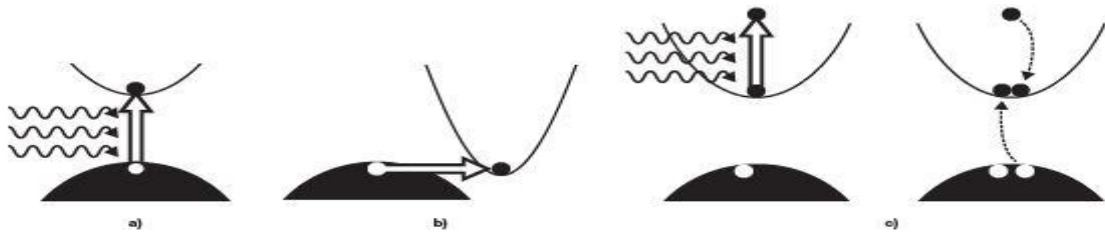


Figure 2.2: Schematic representation of the nonlinear process done during the laser matter interaction, a) Multiphoton absorption, b) Tunnelling ionization, c) Avalanche ionization [56]

2.1.2. Dielectric Response and The Permanent Modification of The Refractive Index

The non-linear absorption process due to the femtosecond laser pulse and dielectric material interaction is generally well understood. However, the mechanism of the permanent modification of the refractive index is complex and depends on the specific materials. Studies are still ongoing on this topic. A fewer possible processes, that may intervene to cause the refractive index modifications, are the following.

A first potential process is color center creation. Femtosecond irradiation results in a significant number of color centers in the material which, are absorptive in the UV wavelength and change the material's refractive index at the wavelengths of interest via the Kramers-Kronig mechanism. Another process is thermal: the energy from the laser melts the substance in the focus volume, and the subsequent rapid re-solidification dynamics freezes the glass in the high temperature state, causing changes in density (and thus refractive index). A third possible mechanism is direct photo-structural change brought on by the femtosecond laser pulses, or reorganization of the structure of chemical bonds in the glass matrix leading to an increase in density. It is challenging to separate the relative contributions of each of the processes mentioned above from one another in real-world scenarios [55].

2.2. Waveguide Writing

Typically, waveguides are written with femtosecond laser with intensity about $1\text{-}5\text{ W/m}^2$, for pulse width of 100 fs correspond to a fluence of $1\text{-}5\text{ J cm}^{-1}$. By appropriately adjusting the scan speed and the repetition rate, such fluences may be achieved with pulse energies ranging from a few μJ to few tens of $n\text{J}$ (for tight, nearly diffraction limited focusing). Depending on whether the pulse period is longer or shorter than the amount of time needed for heat to diffuse away from the focal volume, two distinct femtosecond micromachining regimes can be identified: the low-frequency regime, in which material modification is produced by individual pulses, and the high-frequency regime, in which cumulative thermal effects occur. The change between the two regimes occurs at frequencies of about 1 MHz because the heat diffusion time (heat) out of the absorption volume in the glass is around $1\text{ }\mu\text{s}$ [55].

2.2.1. Writing Configuration

Two alternative writing geometries can be distinguished; longitudinal and transverse, in which the sample is moved parallel to and perpendicular to the beam propagation direction, respectively. The waveguides in the longitudinal geometry are generally symmetric, and their transverse dimension is controlled by the size of the focused spot. A limitation of this method is given by the finite working distance of the focusing objective. On the contrary, in the transverse geometry the sample moves perpendicularly to the laser beam. The working distance of the focusing objective does not limit the length of the waveguides, and optical structures can be fabricated with sufficient flexibility in a depth range of several millimeters, allowing the realization of three-dimensional structures. The limitation of this configuration is that the cross-section of the waveguide can be asymmetric due to the non-unit ratio between depth of focus and spot size [57].

2.2.2. The Repetition Rate and the Thermal Effect

The variable repetition rate of the femtosecond laser pulses is an important parameter in terms of the waveguide characteristics, as it influences the heat accumulation and the thermal diffusion processes that happen during the light absorption by the transparent material. As the repetition rate increases, the time between two consecutive pulses can be shorter. The time needed for the absorbed radiation to diffuse out of the focal volume. As a result, the temperature increases around the focal volume, modifying the material. In general, there are two governing regimes for the repetition rates: low and high repetition rates.

The lower repetition rate regime ranges from 1 to 200 *kHz*, and the time interval between the subsequent laser pulses are longer than the time needed for the absorbed radiation to diverge away from the focal volume. The modification of the dielectric refractive index depends on the interaction within individual pulses, while the arrival of the subsequent pulse will find the material having undergone a full thermal relaxation. The waveguide written with a low repetition rate typically requires lower writing velocity to deposit enough energy, the cross section may be larger than the focal volume. due to heat diffusion which is however present [58][59].

A regime with a repetition rate higher than 2 MHz is called the "high repetition rate regime," where the time interval between the train of laser pulses is so short, even shorter than the thermal relaxation time, that a bunch of subsequent pulses impinging on the focused volume results in a strong heat accumulation [58]. The modified cross section is then far larger than the focal spot.

On the other hand, an intermediate domain with repetition rates ranging from hundreds of *kHz* to a few MHz can be considered. Gradual heat accumulation effects enable the creation of a waveguide with a symmetric and uniform structure while keeping a cross-section more similar to the writing laser's beam waist. The benefits of both high and low repetition rate regimes combine to make this intermediate domain one of the most appealing for femtosecond laser waveguide writing [58].

To gain a clearer understanding of the role of the repetition rate in shaping the waveguide cross section please see figure 2.3.

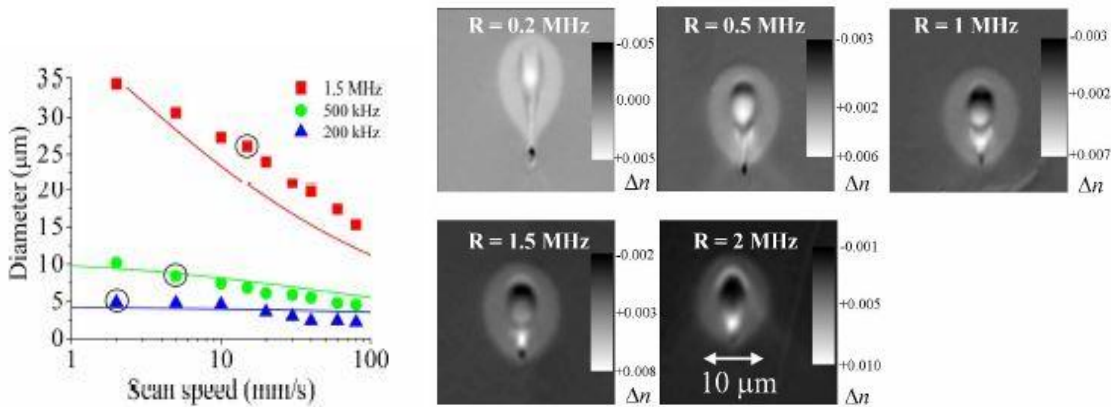


Figure 2.3: On the left, waveguide diameters as a function of writing velocity and repetition rates for 250 nJ of pulse energy, with the continuous line representing the theoretical fit; b) On the right, a microscopical image of the cross-sectional index profile for waveguides written at various repetition rates [59].

2.2.3. Annealing Process

Thermal effects, such as heat accumulation and thermal diffusion, can cause mechanical stress and nonuniform refractive index in the outer region that surrounds the waveguide. This also causes birefringence.

The annealing process is an effective thermal treatment usually used to erase the unwanted outer region and to release the stress. In the case of the Eagle 2000 glass (A borosilicate glass substrate widely adopted for FLM). The glass is heated up to 600 C at a rate of (100° C/h) , then to 750° C at a rate of (75° C/h) , and then cooled down to the room temperature at a rate of (-6° C/h) (Figure 2.4) [58].

During the annealing process, we go through different transition points. Firstly, at a certain temperature (666° C), called the strain temperature, where the stress erasure begins.

Secondly, we reach the annealing point (722° C), in which the internal stresses are rapidly released in a few minutes. Note that the annealing point changes with respect to the glass type [58]. The cooling procedure is kept slow to avoid the insurgence of new stress.

The effect of the annealing process on the refractive index profile is apparent when we see the difference in the image of the waveguide before and after the process (see figures 2.5). In particular the outer ring is completely removed after the annealing treatment, leaving a waveguide with a positive refractive index and a thin black ring with a low refractive index. Annealed waveguides can show lower propagation losses and superior properties (low bending losses) [58].

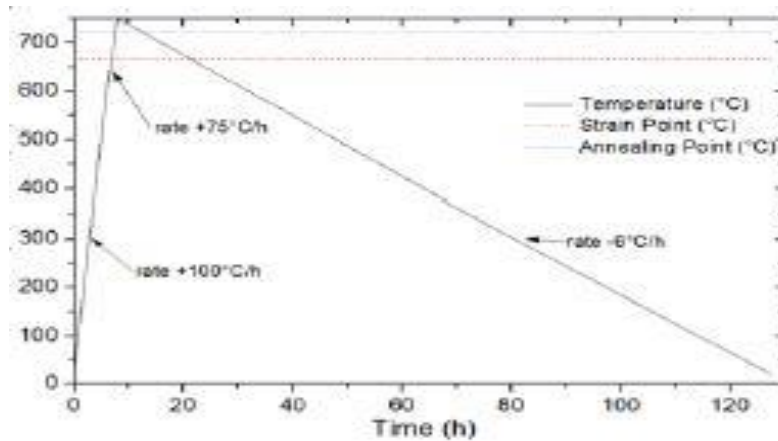


Figure 2.4: Temperature profile of the annealing process, where the dashed red color indicates to the strain point, and the blue line indicates to the annealing point [58].

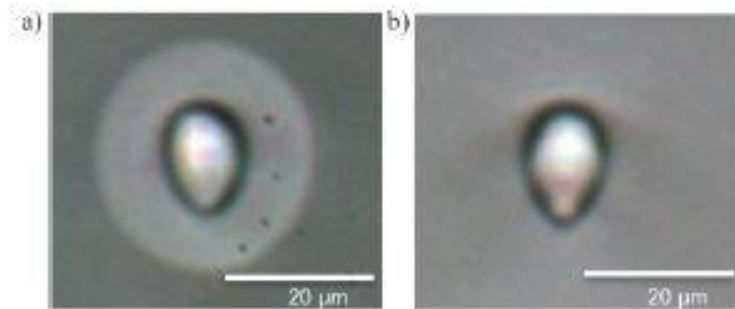


Figure 2.5: Bright field image of a waveguide fabricated in Eagle 2000 glass (a) before the annealing process (b) after the annealing [58].

2.3. State of the Art of 3D Devices

The Femtosecond laser micromachining technique has enabled researchers to realize and engineer complex photonic devices not only in two dimensions but rather in three dimensions. Different passive devices have been implemented, such as power splitters, directional couplers, Mach-Zehnder interferometers, and Bragg gratings, which are the building blocks of complex photonic devices [60][61].

2.3.1. Passive Integrated Photonics Circuits

The directional coupler (1×2 standard beam splitter) consists of two straight waveguides, both brought near to each other to a certain distance called the coupling distance. That allows the power exchange between the two waveguides, where they remain at this interactive distance for a given length called the coupling length (see figure 2.6). The directional coupler either have identical or unidentical arms, where the exponential tail of both waveguides must overlap to have a power exchange by evanescent field interaction.

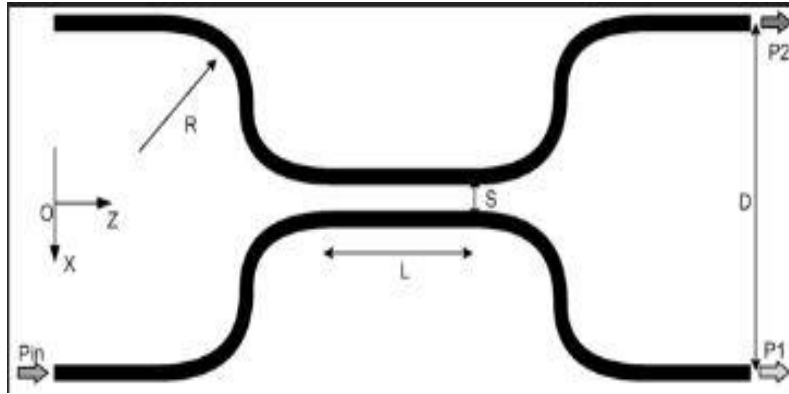


Figure 2.6: Directional coupler of coupling length L , and coupling distance S

As the coupling length increases, the power exchange between the waveguides exhibits sinusoidal behavior. When the two waveguides are identical and the starting power P_0 is localized in the first waveguide, the power exchange as a function of propagation direction z is given by:

$$P_2(z) = P_0 \sin^2(kz) \quad (2.3)$$

$$P_1(z) = P_0 \cos^2(kz) \quad (2.4)$$

Where P_1, P_2 the power in the first and second outputs of the directional couplers, and k is the coupling coefficient that depends on the coupling distance. One can achieve a full power transfer by tuning the coupling length to $L = \frac{\pi}{2k}(2m + 1)$.

Exploiting the FLM for the waveguide fabrication enables us to realize an even more complex structure of beam splitters in 3 dimensions, where we could have many output portals ($1 \times N$). The power splitters of 1×3 were first fabricated in 3D with femtosecond laser written waveguides by the Nolte group, waveguides were fabricated on fused silica by the Ti: sapphire laser system. They have achieved almost an equal splitting ratio (32:33:35) characterized at 1050 nm with splitting losses approaching 6 dB. This potential work has paved the way to use the FLM for the 3D photonics devices realization (see figure 2.7) [62].

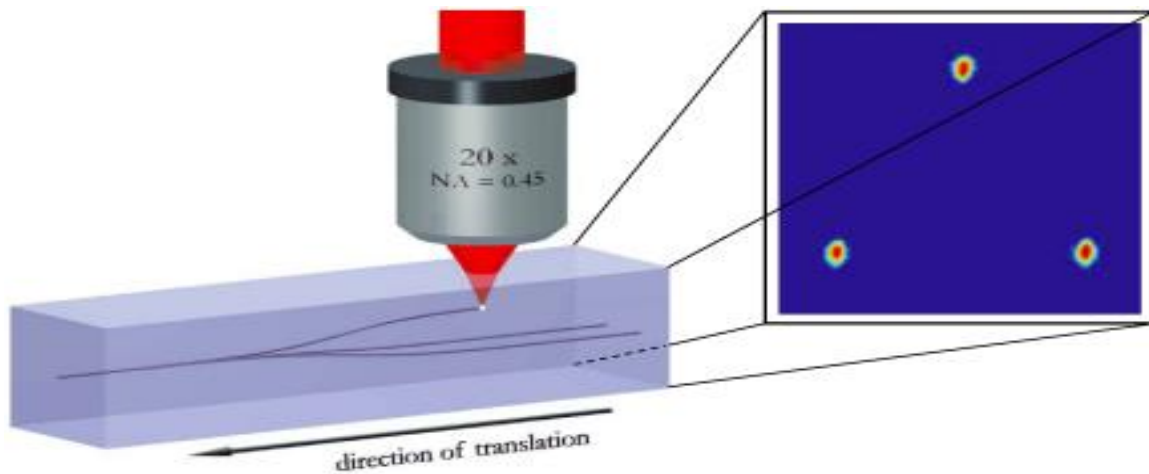


Figure 2.7: Representation of the geometrical shape of 1×3 beam splitter fabricated in three dimension using femtosecond laser, and the CCD image depicts the output powers at each mode [62].

The so-called boson sampling problem is readily solved by photon propagation in a multiport interferometer, inspiring the creation of technology that allow for accurate control of multiphoton interference in large interferometers. An integrated multimode interferometer with arbitrary design of photonic boson sampling was fabricated using the femtosecond laser technique realized by Crespi *et.al* and co-workers (Figure 2.8). By analyzing three-photon interference in a five-mode integrated interferometer they have applied a small instance of the boson sampling problem, supporting the quantum-mechanical hypotheses [70]. This setup can potentially be scaled up to show how quantum systems outperform traditional computers in terms of computing.

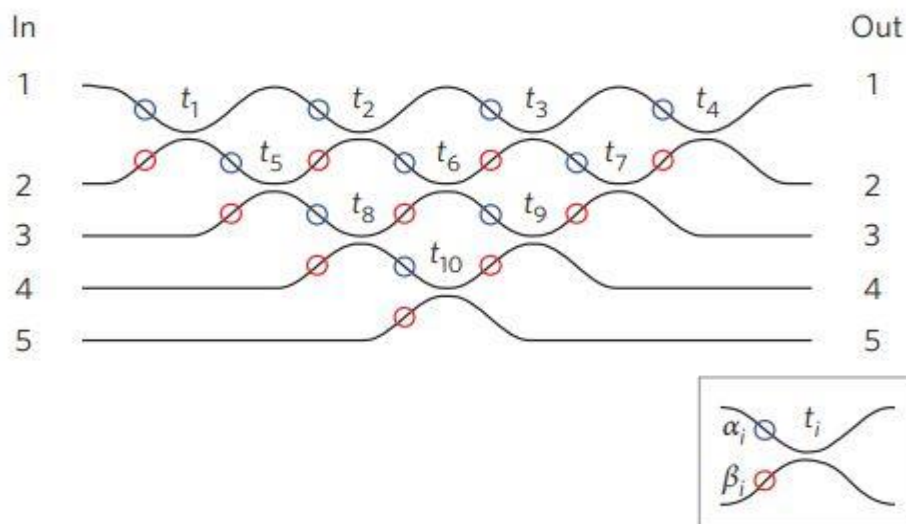


Figure 2.8: Integrated implementation of the scheme presented in the left panel. The circuit comprises five modes, ten directional couplers and ten phase-shifters.

2.3.2. Reconfigurable Photonic devices

The directional coupler is the building component of the complex interferometric devices with high number of modes. The general way to implement an arbitrary unitary transformation is the linear optics which presented by Reck *et al*, who provided a decomposition of a unitary of dimension n as sequence of $n(n - 1)/2$ beam splitters and phase shifters [68].

As another example, three-dimensional multimode interferometers of $n = 4$ and 8 modes were presented in reference [67], to realize the Fourier transformation of the input mode amplitudes (figure 2.9). The authors achieved a fidelity of 0.9822 ± 0.0001 in the amplitude transformation, thus confirming the high quality of the fabrication process [67].

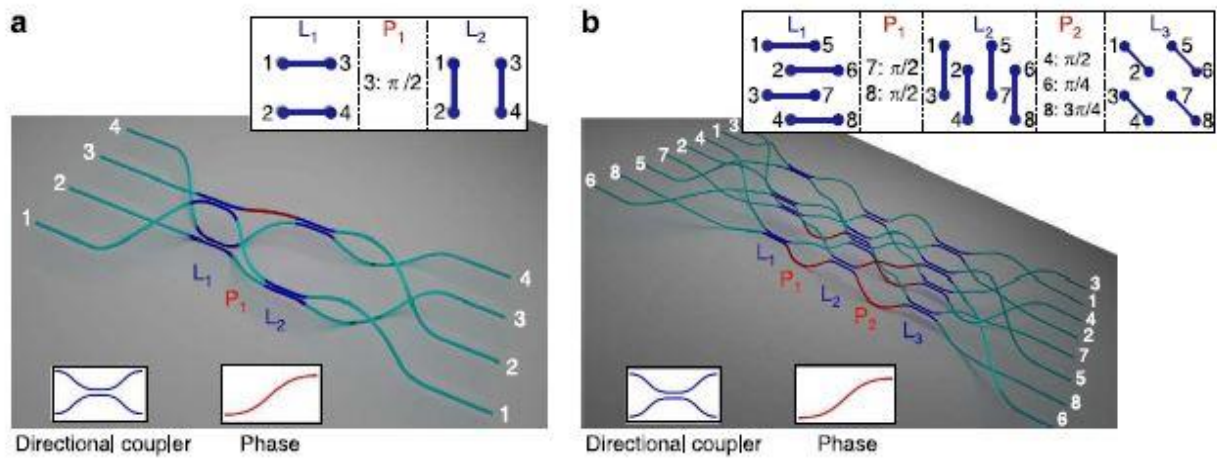


Figure 2.9: Structure of integrated interferometers implementing Fourier transformation fabricated via femtosecond laser in borosilicate glass (a) four-mode interferometer made of four directional coupler and a single phase-shifter (b) eight-mode interferometer made of twelve directional couplers and five phase-shifter [67].

2.3.3. Thermal Phase Shifters

The use of phase shifters based on the thermos-optic effect in photonic circuits allows us to dynamically reconfigure their characteristics, to fine-tune their operation or to create adaptive circuits, considerably widening the application of these devices.

The thermal phase shifters provide an effective strategy to apply a phase shift also on femtosecond laser written photonic circuits. The microheater is created using the following procedure. First a thin metal film is formed on the chip surface, and then the resistors, metal interconnections, and contact pads are laid out by ablating the film using the femtosecond laser that was used to write the waveguides. The use of a gold film is a practical option for microheater construction because gold is not prone to the production of native oxide. By connecting the chip pads to an external power supply system (applying a current), where the temperature is locally diverging inside the glass [69].

The use of the isolation trenches in the glass substrate, can be beneficial to reduce the heat diffusion in the glass, and increase the efficiency of the phase shifters. Furthermore, Francesco *et al* could arrive to a compact microheaters, in which they fabricate them on Mach-Zander

interferometer in alumino-borosilicate, where they were achieved without a loss of the stability or the control of the circuit (see figure 2.10) [69].

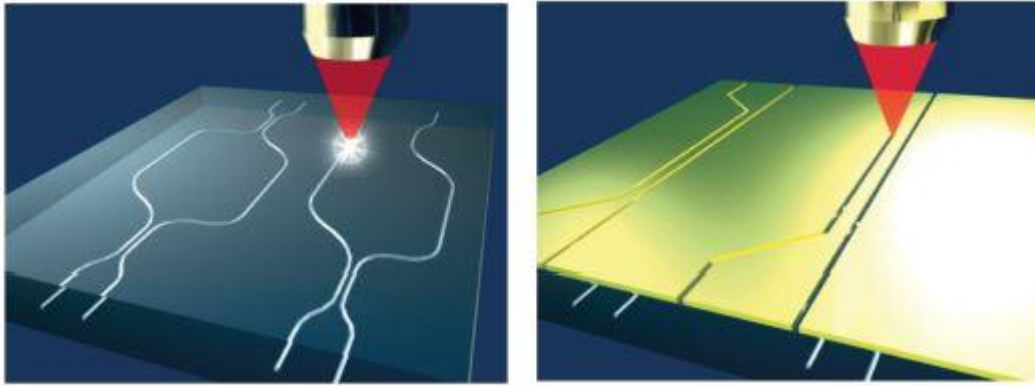


Figure 2.10: 3D section of a reconfigurable MZI, on the left MZI fabricated via femtosecond laser. On the right ablated gold layer on top of the dielectric, in which act as thermal shifter.

2.4. Manipulation of OAM of Light in Femtosecond laser written waveguides

The possibility to shape the wavefront of light beam to a complex intensity pattern such as Laguerre-Gauss mode that carries OAM as we discussed in the previous chapter could be achieved, by exploiting the capability of the femtosecond laser to fabricate and engineer three-dimensional waveguide arrays [56]. Recently, the OAM degrees of freedom has started gaining a huge attention in different fields, ranging from quantum and classical optical communication [63,65] to manipulation of the microparticles and cells [64]. However, implementing a device with bulk optics components and dynamical spatial light modulator to form the complex wavefronts of light requires difficult alignment of the optical setup.

The three-dimensional femtosecond laser direct writing is ideally designed to show OAM mode conversion in a photonic device, presented in ref [71]. The device is made of 12 waveguides in a doughnut cross-section with 4 μm of radius (Figure 2.11). More specifically, the input $\text{OAM}_{\pm 1}$ modes first remain unchanged and then change into their superpositions when the direct-written power is increased. $\text{OAM}_{\pm 1}$ and its superpositions progressively give way to $\text{OAM}_{\pm 2}$ as it is mapped onto the waveguide. The eigenmodes that the waveguide supports effectively determine this mode conversion. Furthermore, by adjusting the direct-written velocity, the input $\text{OAM}_{\pm 1}$ modes may be switched [71][72].

Delivering orbital-angular momentum light behind a single mode optical fiber in combination with a straightforward spiral phase plate construction made using femtosecond 3D direct laser writing is possible up to a topological charge of $l = 3$ (Figure 2.12). These structures effectively create optical vortex beams with orbital angular momentum of $l\hbar$ per photon from out-coupled light from the fiber at a wavelength of 785 nm [73].

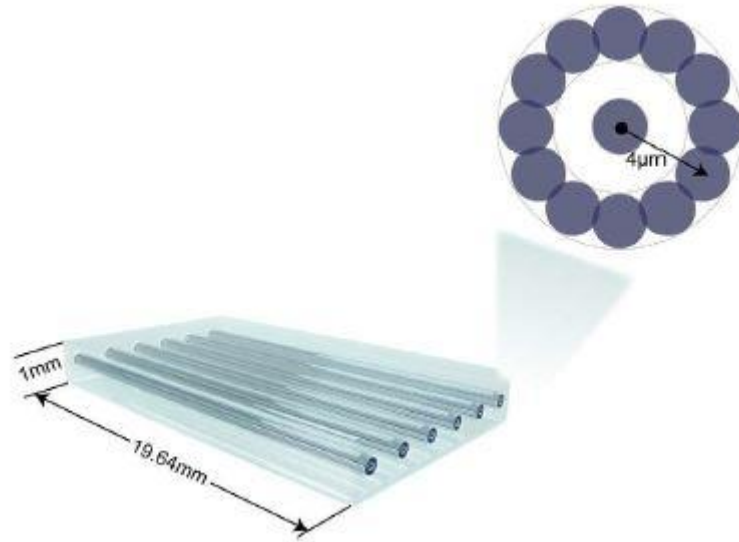


Figure 2.11: representation of femtosecond laser written waveguides. Twelve waveguides are placed at the doughnut cross-section, which has a radius of 4 μm [71].

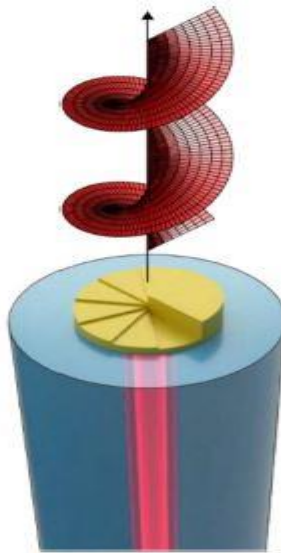


Figure 2.12: A representation of a single mode fiber that delivering OAM beam. Light coupled through a single mode fiber and pass through a spiral phase plate that fabricated at the tip of the fiber via femtosecond laser. This spiral plate generates the beam with a helical phase-front [73].

2.5. Waveguides at Octagonal 2D Cross Section

We can study the far field and near field distribution produced by the output of an array of 8 waveguides placed at the vertices of octagonal shape [3]. The output beam at the near field of each waveguide is approximated as Gaussian profile positioned according to the following equation:

$$R_n = R_0 \cos\left(2\pi \frac{n}{N}\right) \vec{u}_x + R_0 \sin\left(2\pi \frac{n}{N}\right) \vec{u}_y \quad (2.5)$$

Where R_0 is the radius of the polygon. We also consider the phases of the different modes to be arranged as:

$$a_n = 2\pi \frac{n}{N} l \quad (2.6)$$

The arrays will be illuminated with linearly polarized light with a fixed polarization direction. We will further limit our study to the paraxial approximation.

The field of a Gaussian mode at a given propagation coordinate z , and as a function of the transverse position \vec{r} is:

$$g(\vec{r}, z) = \frac{w_0}{w} \exp\left(-\frac{|\vec{r}|^2}{w^2} - ik \frac{|\vec{r}|^2}{2R}\right) \quad (2.7)$$

Where w , and R are the function of the beam radius and the wavefront curvature radius, which depend on the propagation direction z as follows:

$$w = w_0 \sqrt{1 + \left(\frac{\lambda z}{\pi w_0^2}\right)^2}, \quad R = z \sqrt{1 + \left(\frac{\pi w_0^2}{\lambda z}\right)^2} \quad (2.8)$$

The gaussian modes in the array are assumed to be all identical with same radius w_0 (at $z = 0$). The field distribution at arbitrary coordinate z produced by 8 waveguides array can thus be written as:

$$u(\vec{r}, z) = \sum_{n=1}^N \sqrt{I_n} \exp(i \alpha_n) g(\vec{r} - \vec{R}_n, z) \quad (2.9)$$

$$= g(\vec{r}, z) * \sum_{n=1}^N \sqrt{I_n} \exp(i \alpha_n) \delta(\vec{r} - \vec{R}_n) \quad (2.10)$$

where R_n are the waveguides positions at the transverse plane, I_n is the intensity and α_n their phase terms

The propagation and the field distribution of the eight waveguides that were placed at the vertices of a regular octagonal shape were simulated in the near field and the far field (wavelength $\lambda = 808 \text{ nm}$), in which all the waveguides have a mode radius $w_0 = 2.5 \mu\text{m}$. The formation of the vortices in the far field happens due to the constructive and destructive interference, in which the generated vortices change with respect to the integer l forming Laguerre-Gauss mode (Figure 2.13) [3].

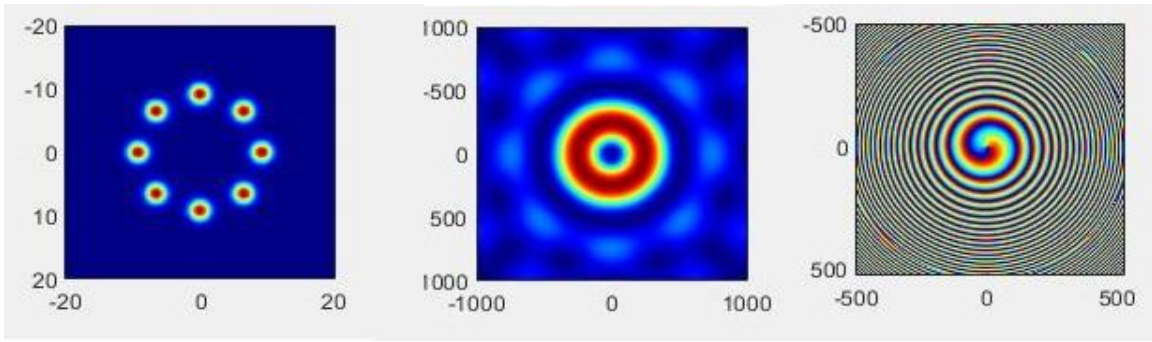


Figure 2.13: Near field (left) and far field (middle $z = 10\text{mm}$) distributions of the waveguides on the vertices of an octagonal shape of integer $l = 1$, where the waveguides have modes diameter of $2w_0 = 5\mu\text{m}$ (illuminated with laser of 808 nm). The interaction distance between the neighboring waveguides is $d = 6.5\mu\text{m}$, and the octagonal radius is $R = 9\mu\text{m}$. On the right the phase applied for each waveguide from $-\pi$ to $+\pi$.

In reference [3], it was shown that a phase singularity is present in the center of the far field distribution which can be approximated as:

$$u(r, \phi, z) \propto r^{|l|} e^{il\phi} \quad (2.11)$$

The expression shows the dependence of the field on the azimuthal angle of order l , similarly to Laguerre-Gauss beams.

3 Experimental Methods

3.1. FLM Apparatus

A schematic representation of the waveguide fabrication setup is shown in Figure 3.1. The setup may be divided into three separate parts: the laser source, the manipulation component of the laser beam, and the motion stages, which enable the sample to be moved in relation to the laser focus, permitting the manufacture of the devices. The laser beam generated by a conversional system (Light Conversion Pharos) passes through an attenuation stage composed of two rotating half-waveplate plates, and a polarizing beam-splitter. A miniature gear-driven rotary stage (AEROTECH MPS75GR) moves the first waveplate; the second waveplate is moved manually.

The microscope objective is used to focus the laser beam in the substrate. In our experiments, we employed a ZEISS 20X Water Immersion objective with $NA = 0.5$. The glass substrate is fixed to a specially designed holder with deionized water inside, which is positioned on a gimbal adjuster. The alignment is carried out using a CCD camera (Edmund Optics) to capture the sample's back-reflected light. The sample and the objective are placed on translational stages, allowing better control of their positions throughout the construction process (Section 3.1.2). To measure the beam power, a power-meter (Ophir Nova II) can be placed in a line before the objective.

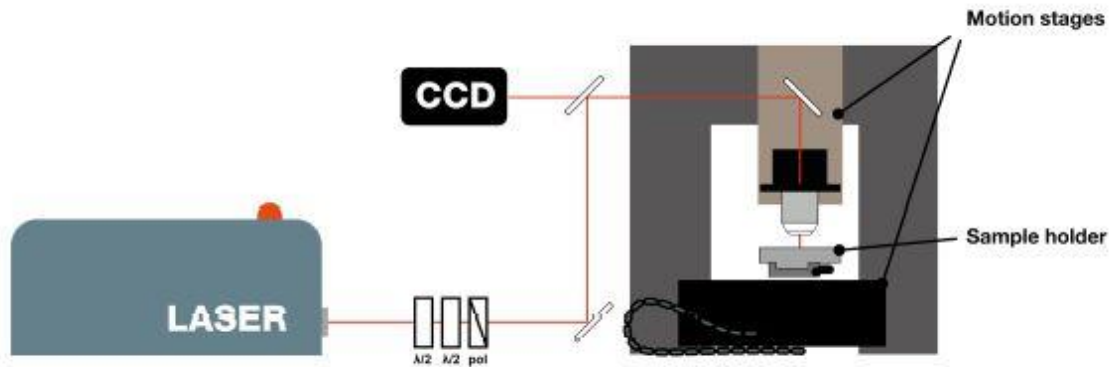


Figure 3.1. The representation of the femtosecond laser setup that used for the waveguide fabrication

3.1.1. The Laser System

The utilized laser is a PHAROS compact commercial femtosecond laser system made by Light Conversion. A Kerr lens mode-locked oscillator make up the system, A stretcher/compressor module, and a regenerative amplifier. The oscillator produces a 76 MHz pulse train with 80 fs duration. The laser cavity is a monolithic aluminum block for stability, and the gain medium is a Yb:KGW (ytterbium doped potassium gadolinium tungstate) crystal that is pumped by laser diodes.

The chirped pulse amplification (CPA) technique is used to amplify the pulse and produce output femtosecond pulses with high energy. The CPA process consists of three stages: a first

stage that expands the pulse's temporal domain; a second stage that amplifies the pulse; and a third stage that back-compresses the pulse duration.

The single diffraction grating employed in the compressor module may be manipulated (moved) to introduce positive or negative chirp, which can be used to fine-tune the pulse width. A Yb:KGW crystal serves as the foundation for the regenerative amplifier, which is pumped by two continuous-wave solid state laser diodes.

The system delivers at the output sub-190 fs pulses with a peak pulse energy of 0.2 mJ and a central wavelength of 1030 nm. One may adjust the repetition rate from a single shot to 1 MHz.

3.1.2. Motion stages

Three linear translators along the x , y , and z directions make up the motion stages. The motion stage (AEROTECH ABL1500Z-050) that moves the objective controls its position along the z -coordinate and enables movement of the focus into the substrate during fabrication. The maximum travel range of this stage is 50 mm, and its maximum speed and acceleration are 300 mm/s and 20 m/s², respectively. Its nominal resolution is 100 nm. The sample is moved in the plane perpendicular to the laser beam by two stages, the AEROTECH ABL1500WB-200 for the x -direction and the AEROTECH ABL1500-100 for the y -direction. The maximum travelling distances in x and y directions are 100 mm and 200 mm, respectively, with a nominal 100 nm precision. For both stages, the maximum speed and acceleration are 2 m/s and 20 m/s², respectively.

The stage driver also sends a signal to the laser system, enabling switching on and off the laser beam via its internal shutter. The stages may be programmed using G-code scripts and are managed by a computer running a proprietary piece of software called the AEROTECH CNC Operator Interface.

3.2. Post-Processing and Visual Inspection

The Annealing process of the sample was performed using a muffle furnace called Nabertherm, type LV 5/11/B180. The oven has a cured vacuum fiber module liner that is extremely robust, and a stainless-steel sheet with a texture serves as the casing (non-rusting design). For stability and low external temperatures, the case is double walled. The oven's temperature homogeneity is good with a solid-state power control relay with no noise and more than six air changes per minute due to the preheating of incoming air.

The facet conditions have a significant impact on light coupling in the femtosecond written waveguides. The input and output sides of the waveguides always have glass chipping, surface flaws, and roughness after they have been fabricated. It is common practice to do surface polishing on the glass facets to lower scattering losses, and increase coupling efficiency. A polishing machine is used for this procedure, which employs rotating abrasive disks. In order to achieve optical-grade polishing, the sample is positioned perpendicular to the moving disk and a series of abrasive disks with decreasing roughness is used.

Assessing the results of the fabrication or glass-processing procedures requires the glass sample to be visually examined with a microscope after laser irradiation. To this purpose we use a

Nikon ECLIPSE ME600 microscope equipped with an image-capturing PixeLINK PL-B871 CCD camera. The microscope can mount four different objectives: 4X, 10X, 20X, and 40X. A top view of the glass sample enables inspection of the overall waveguide geometry as well as the detection of irradiation track damages and disruptions. High losses result from these disruptions, and in some situations, the guiding properties of the inscribed structures are harmed. They are often brought on by the presence of particles, including dust, which locally alter the laser focus on the manufacturing surface.

The input and output interfaces quality and roughness may be examined by looking at the lateral facets. This examination is particularly helpful following the polishing process or when performing a visual study of the waveguide cross-sections. When writing waveguides with varied irradiation settings or comparing structures before and after annealing, the latter approach is also helpful for comparing cross-sections.

3.3. Optical Characterization Method

Waveguide characterization is performed by coupling laser light. Measurements can evaluate the power distribution at the output ports, the waveguide losses, and the mode profile. The laser diodes that generate the coherent light employed for characterization have a wavelength of 808 nm.

The so-called fiber coupling (or end-fire coupling) setup is used for all the optical characterization investigations presented in this thesis (see figure 3.2). It entails connecting the fiber's distal end with the waveguide's input facet in order to couple light from an optical fiber directly into the integrated optical device. First, a microscope objective is used to couple the laser source's free-space coherent light to the single mode fiber. The other end of the fiber is peeled and cleaved, and the fiber tip is moved as near as feasible to the integrated waveguide's input.

An objective collects the light that is emitted from the integrated circuit and directs it toward a power meter (such as the Ophir NovaII, or Anritsu ML9001A) or a CCD camera (such as the Edmund OpticsEO-1312M). A submicrometric positioning mechanism is used to regulate the relative position of the sample and the fiber tip: The fiber and the objective are mounted on Melles Griot NanoMAX stages, and the sample is placed on a Thorlabs MBT40 four-axis micro-positioner.

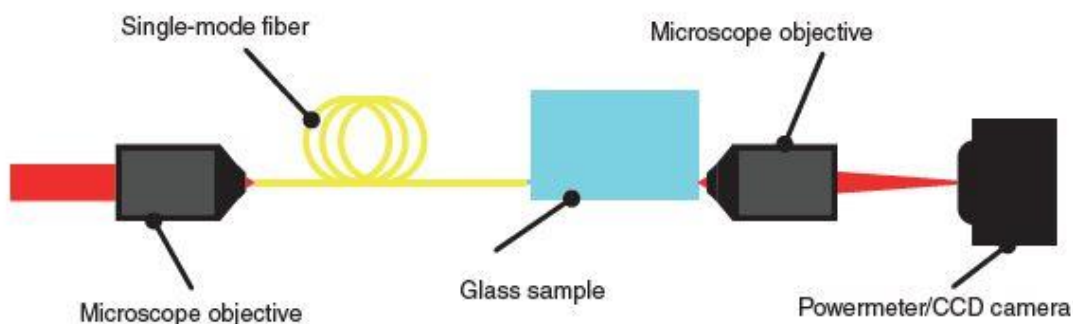


Figure 3.2: Representation of end-fire fiber waveguide coupling

3.3.1. Waveguide's Mode Profile

The confinement characteristics of the waveguides may be determined by taking measurements of the mode profile. End-fire coupling is used to couple the light in our waveguide, and the CCD camera captures both the waveguide's and fiber's end facet, using the same magnification. The photos of the modes are captured using the CCD's proprietary software while taking care not to oversaturate the sensitive pixels. Mode profiling may be used to assess the symmetry of the waveguide, determine if the waveguide is single-mode or multi-mode, and calculate coupling losses.

3.3.2. Losses Characterization

Waveguiding structure unavoidably introduce optical losses. Any photonic application requires their characterization, but it becomes considerably more important when working with quantum photonics experiments that rely on single photon inputs. Using the equipment described in the preceding section, laser femtosecond laser written waveguides are characterized.

To demonstrate optical loss, one starts by measuring the device's overall losses by comparing input and output power. Insertion loss is defined as:

$$IL|_{dB} = -10 \log_{10} \left(\frac{P_{out}}{P_{in}} \right) \quad (3.1)$$

where P_{out} is the measured output from the waveguide or photonic device and P_{in} is the measured input power from the optical fiber.

Several distinct factors all contribute to the IL, including:

- **Fresnel Losses (FL)**

The refractive index mismatch at the air-glass interface (contact) results in some light back-reflection, which causes losses known as FL. Assuming normal incidence, which applies to all observations in this thesis, the interface's reflectance may be calculated as follows:

$$R = \left(\frac{n_G - n_{air}}{n_G + n_{air}} \right)^2 \quad (3.2)$$

where n_G and n_{air} are the refractive indices of the two media (glass and air). The FL as function of R that represents the reflectivity result to be:

$$FL|_{dB} = -10 \log_{10}(1 - R) \quad (3.3)$$

To consider both input and output facets, this term has to be taken twice.

- **Coupling losses**

Coupling losses (CL) are due to a single-mode optical fiber's mode and a femtosecond laser written waveguide's mode not matching up. The waveguide and fiber mode electric field distributions f_{WG} and f_F are used to calculate the CL. The CCD camera is used to capture the intensity profiles of the fiber and the waveguide while maintaining a constant distance between the objective and the camera, to get a constant scaling factor. For a single mode waveguide or fiber, it is possible to determine the electric field

distribution $f(x, y)$ from the intensity profile of the mode. In fact, because the basic mode lacks sign inversions, the electric field distribution in the xy plane, is given by:

$$f(x, y) = B \sqrt{I(x, y)} \quad (3.4)$$

CL is thus evaluated numerically as:

$$CL|_{dB} = -10 \log_{10} \left(\frac{|\iint f_{WG} f_F dx dy|^2}{\iint |f_{WG}|^2 dx dy \iint |f_F|^2 dx dy} \right) \quad (3.5)$$

Where B is a constant with an actual value, and $I(x, y)$ is the measurement intensity profile.

- **Propagation Losses**

Propagation losses (PL) are losses per unit length resulting from light propagation inside the waveguide. These are estimated by subtracting the other contribution from IL.

$$PL|_{\frac{dB}{cm}} = \frac{IL|_{dB} - CL|_{dB} - 2FL|_{dB}}{L} \quad (3.6)$$

Where L is the length of the straight waveguide. Another method for directly characterizing PL would be measured to the output power for a set of waveguide lengths, after repeatedly cutting the sample. This method was not used in this thesis work.

Additional losses are introduced by curves in the WG path. The loss terms, known as bending losses (BL), result from the guided mode's distortion in the curved waveguide. It is calculated by evaluating the losses of equivalent straight and curved waveguides as follows:

$$BL|_{\frac{dB}{cm}} = \frac{IL|_{dB, SWG} - IL|_{dB, BWG}}{L_s} \quad (3.7)$$

$IL|_{dB, SWG}$ and $IL|_{dB, BWG}$ are the insertion losses measured for the straight waveguide and the bent waveguide of the same length, respectively, and L_s is the length of the curved path.

According to a theoretical model, the bending loss term behaves exponentially with respect to the radius of curvature [74]:

$$BL|_{\frac{dB}{cm}} = A \exp(-BR) \quad (3.7)$$

where R is the radius of curvature and A and B are parameters that depend on the characteristics of the waveguides.

4 Optimization of Waveguides and Directional Couplers

In this chapter we present the experimental optimization process of femtosecond laser written waveguides and the characterization of directional couplers devices, aiming to achieve low optical losses and control of the coupling parameters between adjacent waveguides.

4.1. Optimization of Waveguides

Waveguide optimization could involve in principle many inscription parameters. Here we concentrated on the writing velocity and beam irradiation power. These two factors are simple to manipulate and have been shown to be very effective in the literature. The values of the other parameters were instead taken from the literature, or from the research-group experience with the same substrate.

The setup mentioned in the preceding chapter was used to fabricate waveguides. The pulse duration was set at 170 fs and the laser repetition rate was 1 MHz. Alumino-borosilicate glass samples that were 1 ± 1 mm thick had waveguides fabricated onto them (EagleXG, Corning). Additionally, all waveguides were fabricated at a depth of 60 μm . This in fact would possibly boost the effectiveness of thermal phase-shifters, since waveguides need to be close to the surface in order to perform an efficient modulation of the refractive index and maintain low power dissipation.

The use of the multi-pass approach, which employs numerous overlapped laser scans, allowed for the creation of waveguides with a larger index contrast. Additionally, this method enhances the waveguide's confinement qualities, which is beneficial for achieving lower bending radii and more compact devices [58].

4.1.1. Coupling and Propagation Losses Optimization

The waveguides were fabricated with several writing velocities ranging from 15 m/s to 30 mm/s, exploring a wide range of values for the irradiation power varies from 200 mW to 380 mW, and a fixed number 6 of overlapped scans. The waveguides were characterized using a laser diode at 808 nm wavelength and the apparatus described in the previous section 3.3. Using the techniques described in Section 3.5.1, we measured IL for all waveguides; see Figure 4.1.

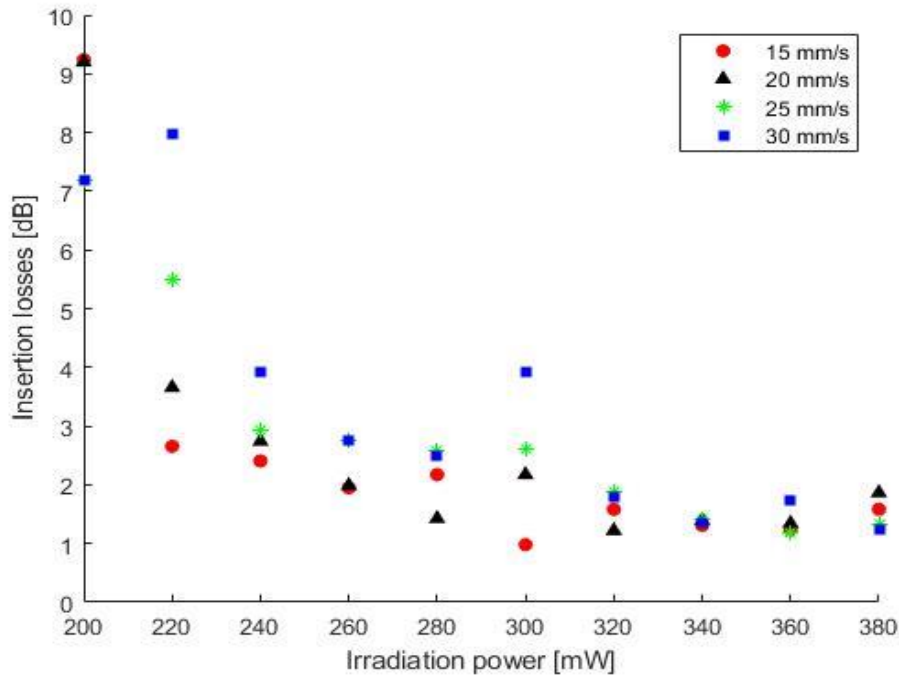


Figure 4.1: IL as function of the irradiation power of femtosecond written waveguides fabricated with four different writing velocities 15, 20, 25, and 30 mm/s.

We also separated the distinct loss factors, with CL and PL presented in detail as follows:

- **CL**

Evaluating the overlap integral that mentioned in section 3.5 between the single-mode fiber's mode (780HP, ThorLabs) and the written waveguides. Results are reported (Figure 4.2.a).

- **PL**

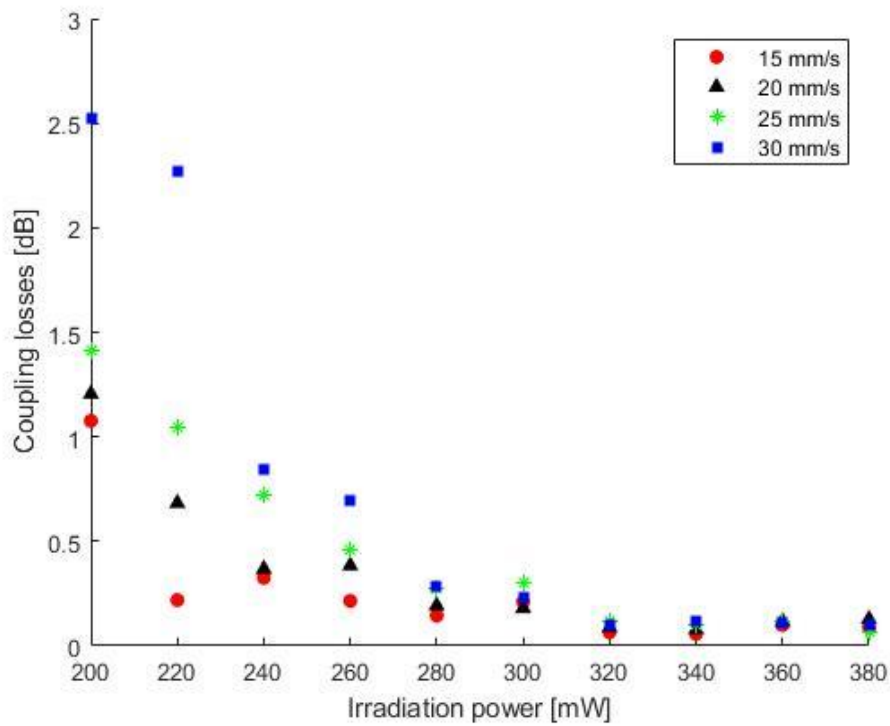
We calculated the PLs for all the waveguides using the mathematical formula that introduced in Section 3.5 considering 0.035 dB as FL. Results are reported in Figure 4.2b

We note that PLs are about 0.5 dB/cm for all writing velocities with 340 mW of irradiation power. In fact, the IL are typically identical for these waveguides written with 340 mW.

In addition, waveguides written with a 15 mm/s writing velocity and an irradiation power above 300 mW show lower coupling losses and propagation losses.

As a result, we chose as the optimal waveguides are the ones fabricated at 340 mW since they have identical amounts of insertion losses for all the writing velocities (see Table 4.1). In fact, varying the writing velocity may be useful to tune that waveguide propagation constant β and thus gain advanced control on waveguide coupling.

(a)



(b)

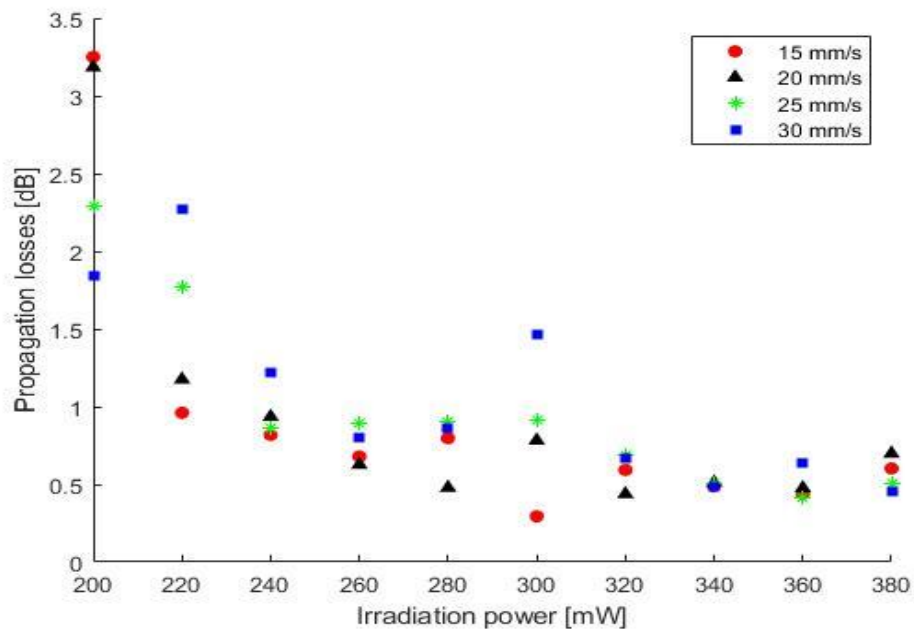


Figure 4.2: Femtosecond laser written waveguides were fabricated within four different velocities. (a) CL [dB] (b) PL [dB/cm] both plotted versus the irradiation power.

	IL [dB]	CL[dB]	PL[dB/cm]
15mm/s	1.32	0.05	0.49
20mm/s	1.39	0.07	0.51
25mm/s	1.40	0.09	0.51
30mm/s	1.36	0.11	0.48

Pulse Duration	170 fs
Irradiation Power	340 mW
Scans	6
Fabrication Depth	60 μ m
Repetition Rate	1 MHz

Table 4.1: Table in the left shows the ILs, CLs, and PLs of the optimal waveguides that written with 340 mW of irradiation power. In the right table the fabrication parameters are highlighted.

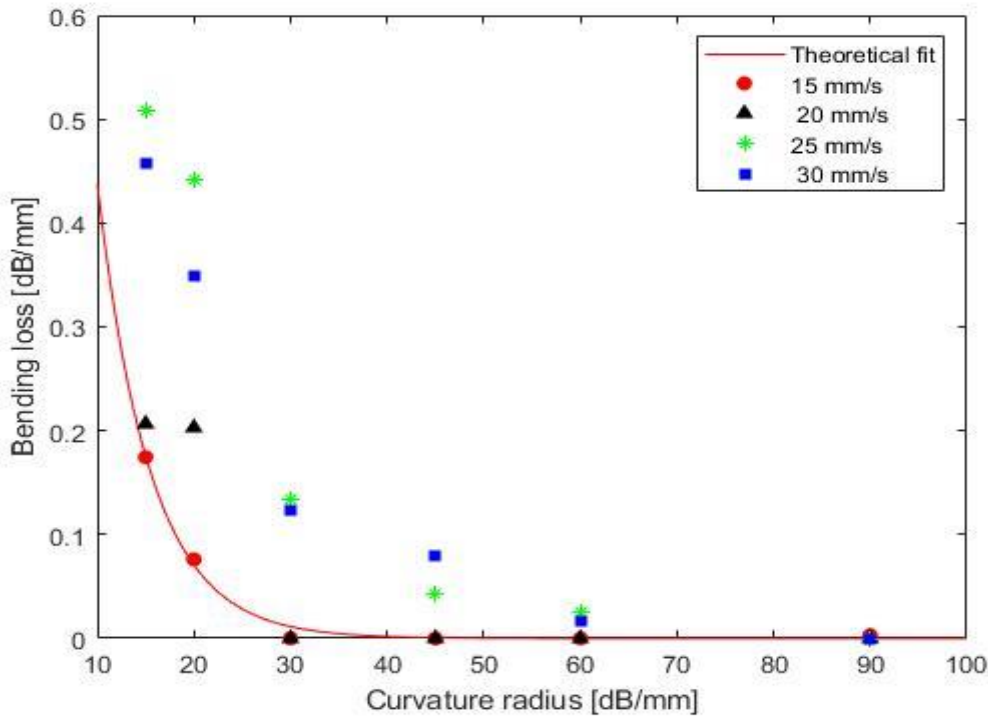


Figure 4.3: Bending Losses of femtosecond laser written waveguides fabricated with four writing velocities 15, 20, 25, and 30 mm/s characterized as function of the curvature radius.

4.1.2. Characterization of Bending Losses

Radiation losses, known as bending losses, result from the guiding path's curvature along the propagation direction. A single-mode waveguide's mode profile is distorted in the curved region, and the field is pushed outwards. Light radiates out from the core region as a result of an increase in coupling with the cladding modes. As the radius decreases for the circular bends, these losses grow exponentially.

We fabricated S-bends (two successive circular arcs producing an S-shaped waveguide) with bending radii varying from 15 mm to 90 mm, and several writing velocities. The same total curved length was kept for all waveguides. Additionally, straight waveguides were realized, enabling the reference measurement of IL and retrieval of the bending losses using Equation (3.9). We noticed that for curvature radii greater than 45 mm, measured bending losses were negligible (Figure 4.3).

4.2. Directional Couplers Characterization

Characterizing the coupling parameter is a crucial stage in the design and implementation of our device. To achieve this, we analyze the experimental results, but first we should offer a brief theoretical background on coupled mode theory for two close waveguides.

4.2.1. Coupled mode theory

We consider two guiding regions that are not too close to one another; this approximation is known as the weak coupling condition. This assumption allows us to think of the dielectric structure as being made up of two separate waveguides, which are responsible for guiding a single mode and have their own refractive index distributions ($n_1(x, y)$ for the first, and $n_2(x, y)$ for the second). We refer to the modes that are guided by the first and second waveguides, respectively, as ψ_1 and ψ_2 . A general field distribution in the overall structure is expressed as the superposition of these two fundamental modes using appropriate coefficients that depend on the position along the propagation direction z :

$$\psi = A_1(z)\psi_1(x, y)e^{-j\beta_1 z} + A_2(z)\psi_2(x, y)e^{-j\beta_2 z} \quad (4.1)$$

where β_i is the propagation constant in the i -th waveguide and A_i is the amplitude term that depends on the propagation coordinate z .

One can study the evolution of $A_i(z)$ using the coupled-mode equations that are written as follows:

$$\begin{cases} \frac{dA_1}{dz} = -jk_{11}A_1 - jk_{12}A_2e^{j\Delta\beta z} \\ \frac{dA_2}{dz} = -jk_{22}A_2 - jk_{21}A_1e^{-j\Delta\beta z} \end{cases} \quad (4.3)$$

where $\Delta\beta$ is defined as $\Delta\beta = \beta_2 - \beta_1$ and k_{ij} is the coupling coefficient. The following overlap integral is used to define:

$$k_{ij} = \frac{k_0}{2n_i} \frac{\iint \psi_i^* \Delta n_j^2(x, y) \psi_j dx dy}{\iint \psi_i^* \psi_j dx dy} \quad (4.4)$$

For $i \neq j$ the coupling coefficient is related to an overlapped integral averaged over the perturbation term of the refractive index Δn_j^2 . Typically, the coupling coefficients of $i = j$ are negligible.

The square of the refractive index of the overall guiding structure can be written as the superposition of the squares of the refractive indices of the two unperturbed structures:

$$n^2(x, y) = n_j^2(x, y) + \Delta n_j^2(x, y) \quad (4.5)$$

Where Δn_j is the difference between the refractive index of the waveguide j and the refractive index of the generic point (x, y)

Defining the vector $\mathbf{A}(z) = [A_1(z), A_2(z)]$ allows to write the equation in a more compact form as follows:

$$\frac{d\mathbf{A}}{dz} = -i\mathbf{M}(z)\mathbf{A} \quad (4.6)$$

Where the matrix \mathbf{M} is defined as follows:

$$\mathbf{M}(z) = \begin{pmatrix} k_{11} & k_{12}e^{j\Delta\beta z} \\ k_{21}e^{-j\Delta\beta z} & k_{22} \end{pmatrix} \quad (4.7)$$

For two identical waveguides, one has $\Delta\beta = 0$, $k_{ij} = k_{ji} = k$, and $k_{ii} = k_{jj} = 0$, and Equation (4.2) is simplified as follows:

$$\begin{cases} \frac{dA_1}{dz} = -jk A_2 \\ \frac{dA_2}{dz} = -jk A_1 \end{cases} \quad (4.8)$$

$P_i(z) \propto |A_i(z)|^2$ provides the power distribution at a specified z -coordinate. The first order linear differential equations formula [75] may be used to find the solution of (4.6):

$$\mathbf{A}(z) = \mathbf{A}(z_0) \exp\left(-j \int_{z_0}^z \mathbf{M}(s) ds\right) \quad (4.9)$$

The powers at the output of the waveguides are written in the following ways:

$$|A_i(z)|^2 = P_i(z) \quad (4.10)$$

$$P_2(z) = \sin^2(kz) \quad (4.11)$$

$$P_1(z) = \cos^2(kz) \quad (4.12)$$

The P_i represents the power at the first and the second waveguides as function of the propagation direction z and the coupling coefficient k .

4.2.2. Directional Couplers

The directional coupler is slightly different from the two parallel waveguides, in which the two waveguides are brought smoothly close to each other for a certain length L . The two waveguides are kept in distance as well called the coupling distance d as presented in Section 2.3.1. The Transmissivity of the directional coupler due to the evanescent coupling between the two arms is expressed in the following formula:

$$T = \sin^2(kz + \Phi) \quad (4.12)$$

where $\Phi = k \sqrt{\frac{\pi R d_0}{4}}$ is a term that accounts for this extra coupling impact in the curving part and k is the coupling constant, where it decays exponentially with the coupling distance d , since it depends on the overlap integral of the exponential tails of the fundamental modes of the separate waveguides.

Since the coupling constant k depends on the overlap integral of the exponential tails of the fundamental modes of the different waveguides, it decays exponentially with the coupling distance d .

$$k(d) = k_0 e^{-\frac{d}{d_0}} \quad (4.13)$$

Where k_0 and $\frac{1}{d_0}$ are positive coefficients that belong to the characteristics of the waveguides. the parameter d represents the distance between the directional coupler's arms at the interaction region.

The free parameters one can optimize to reach the desired splitting ratios are the coupling length L and the coupling distance d as defined in Section 2.3.1.

As a first test, we fabricated a series of directional couplers with a fixed coupling length of 2 mm and a coupling distance d that varies from $4\mu\text{m}$ to $10.5\mu\text{m}$. Waveguides were written with 340 mW power and 15 mm/s of writing velocity at 6 μm below the substrate surface. The results of the characterization of the bending losses are utilized to determine the bending radius for the directional couplers (see Section 4.1.2). Larger bending radii make the footprint of the final device bigger, leading to an increase in losses due to the longer propagation. Using lower radii, on the other hand, results in large bending losses and could raise the overall losses as well. We have chosen to fabricate the directional coupler with a bending radius of $R = 45$ mm in order to deal with this trade-off. We computed the experimental transmissivity of the directional couplers as:

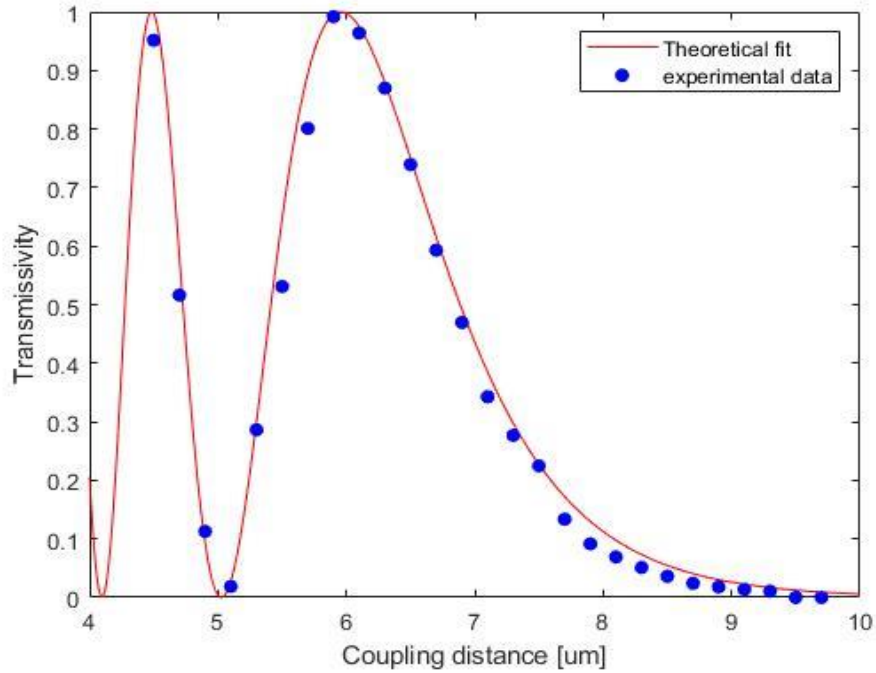
$$T = \frac{P_2}{P_1 + P_2} \quad (4.14)$$

Where P_1 and P_2 are the power values measured at the output of the first and second waveguides respectively.

The observations of the experimental data are plotted in Figure 4.4a. We fitted Equation (4.12), having the coupling distance d as free parameter. The theoretical model and the experimental data showed good agreement, which attests to the quality of the waveguides and the stability of the directional couplers.

Moreover, by further using Equation (4.12), we could retrieve the coupling coefficient k that has an exponential decay with the coupling distance (Figure 4.4b), which fits the theoretical expression in Equation (4.13), with certain coefficients k_0 and $\frac{1}{d_0}$.

(a)



(b)

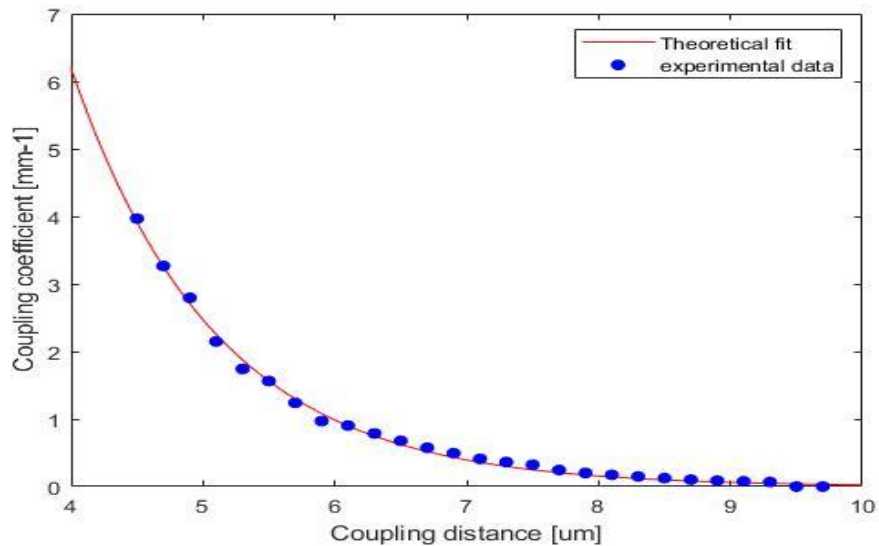


Figure 4.4: (a) The transmissivity as function of the coupling distance d . (b) The coupling coefficient k as function of the coupling distance d . The red line represents the theoretical fit, and the blue points are the experimental data.

As a further analysis, we experimentally explored the waveguides detuning using directional couplers. The transmissivity of directional couplers with unidentical arms could be derived without the assumption that we adopted in Equation 4.7. Accordingly, we have $\Delta\beta \neq 0$, which indicates that the two arms are different, and $k_{ij} = k_{ji} = k(d)$. The Equation (4.12) is extended as follows:

$$T = \frac{1}{1 + \left(\frac{\Delta\beta}{2k}\right)^2} \sin^2 \left(kL \sqrt{1 + \left(\frac{\Delta\beta}{2k}\right)^2} + \Phi \right) \quad (4.13)$$

Where $\Delta\beta$ represents the detuning between the arms of the directional couplers.

We have fabricated a set of directional couplers of identical arms with a fixed coupling distance $d = 6 \mu\text{m}$ and varying the coupling length L from 0 mm to 4.5 mm. The waveguides were fabricated with 340 mW power and 15 mm/s of writing velocity. The purpose of this set of the directional couplers was aiming to retrieve the coupling coefficient k .

The experimental results are plotted in Figure 4.5b. We fitted Equation (4.12) having the coupling length L as free parameter. The retrieved coupling coefficient was $k = 1.15 \pm 0.02 \text{ mm}^{-1}$.

The major fabrication was intending to explore the detuning parameter, furthermore we have fabricated a set of directional couplers with a fixed coupling distance of $d = 6 \mu\text{m}$ and a coupling length of $L = 3.35 \text{ mm}$. In this devices we fabricated unidentical arms of directional coupler by varying the writing velocity of one arm from 15 mm/s to 30 mm/s, where the other arm is fabricated with a fixed writing velocity of 15 mm/s.

The Transmissivity of the directional coupler was plotted as function of the writing velocity difference ΔV between the arms of the directional couplers (Figure 4.5a). The Equation (4.13) was fitted using ΔV as free parameter.

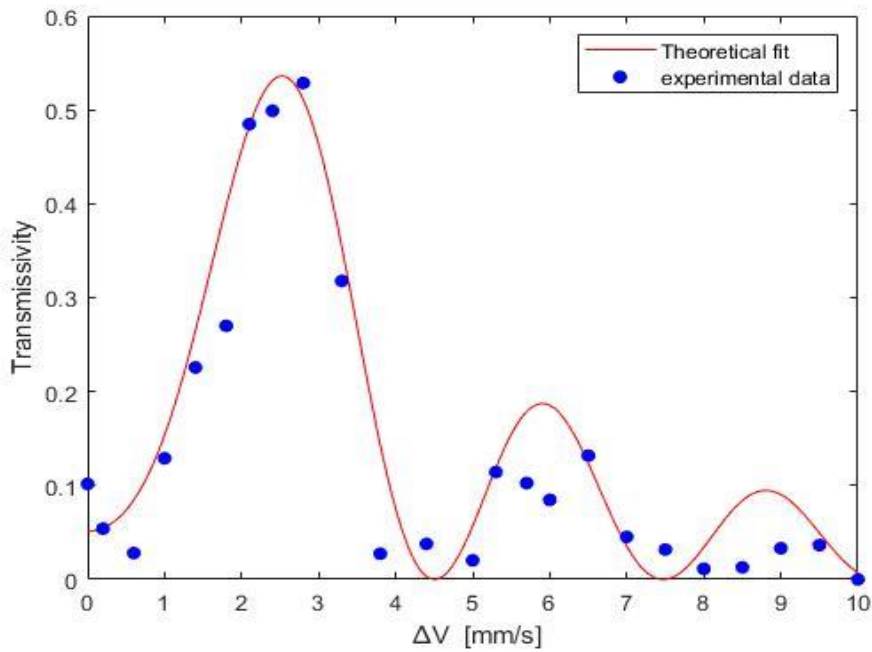
The observations of the experimental data and the theoretical model (Eq 4.13) showed good agreement, which proves that the writing velocity is a strong parameter to detune the waveguides of the directional coupler. Moreover, the detuning factor $\Delta\beta$ could be written as a function of the writing velocities of the directional coupler arms as follows:

$$\Delta\beta = C|V_2 - V_1| = C\Delta V \quad (4.14)$$

Where C is a coefficient that depends on the characteristics of the waveguides, V_i represents the writing velocity of the i -th. From the theoretical fitting the coefficient value is retrieved $C =$

$0.40 \pm 0.01 \text{ mm}^{-2}\text{s}$. By using these information, the design of the final device is discussed in the next chapter.

(a)



(b)

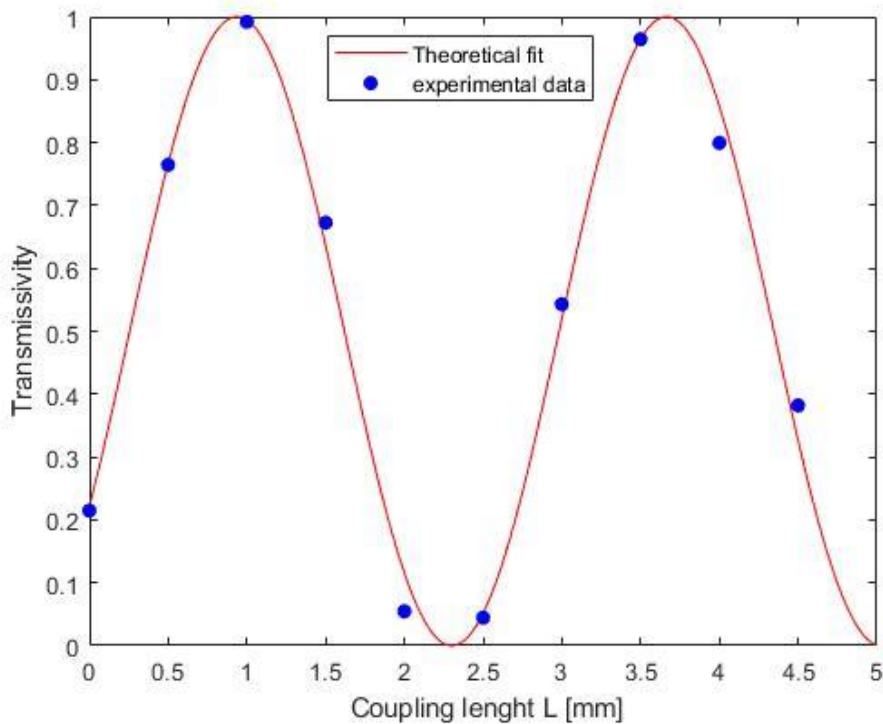


Figure 4.5: (a) The transmissivity of the directional couplers as a function of the writing velocities difference of the two arms ΔV . (b) Transmissivity as function of the coupling length L . The red line represents the theoretical fit and the blue points are the experimental data.

5 Fabrication of Three-Dimensional Waveguides in Octagonal Configuration

In the chapter we present the optimization steps for the design of the layout presented in section 2.5, where eight waveguides are placed at the vertices of an octagonal lattice. We have carried out the fabrication and the characterization of an integrated-optics circuit implementing that scheme. Crucially, the waveguides must be close together in the octagonal arrangement, with negligible coupling of light among them.

5.1. The Geometrical Design of the Device

The aim of the experimental work in this thesis is the realization of eight planer waveguides transformation into a two-dimensional cross section. The eight waveguides are placed at the vertices of an octagonal configuration with interaction distance d between the vertices, and radius of the octagonal R (Figure 5.1)

The final device's geometrical configuration was engineered and designed with various constraints in mind, such as geometrical constraints where the device's arms must not intersect (cross) with each other and device miniaturization, where it is required to use the minimal reliable bending curvature to achieve less propagation and bending losses. Having eight waveguides at the vertices of an octagonal cross section is not straightforward, because we have to note that the subsequent fabrication of the waveguides at the same cross section must not affect the rest of the waveguides.

The out-of-plane bend segments of both layouts were realized with a sine-squared function that provides smooth transitions.

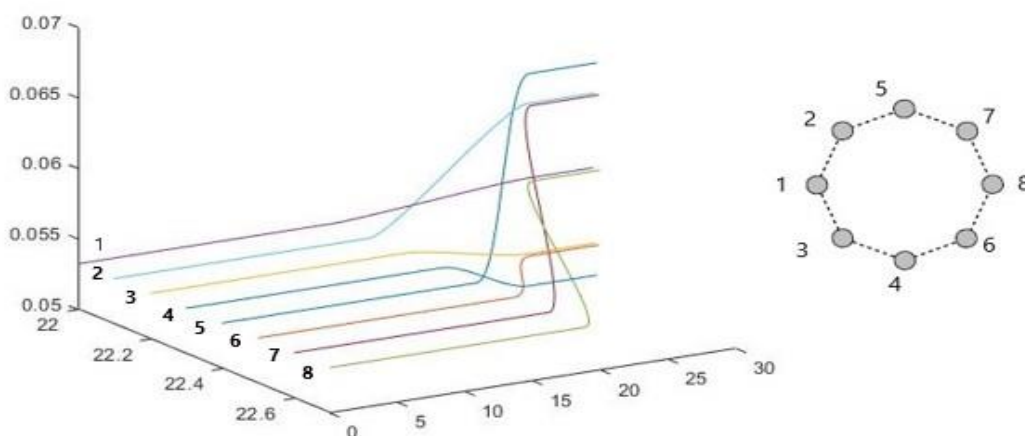


Figure 5.1: Geometrical configuration of the final device, where the transition of the eight waveguides into a vertices of a regular octagonal shape is arranged according to a specific ordering.

The transition from the 8-waveguides in a plan configuration into the octagonal cross section is realized with a point-to-point representation using a custom MATLAB script that generates the entire series of points that control the motion stages during the fabrication.

The motion stage drivers can manage a finite number of points per second. The translation velocities were determined in Section 4.1, ranging from 15 mm/s to 25 mm/s. We have used a proper points-per-second density (200 commands per second) that allows accurate representation of the curved segments without saturating the motion stage capabilities.

5.2. Propagation of Eight-Waveguides

The waveguides of the device must sustain the input power during the propagation. The version of the transformation circuit proposed in ref [3], proven that the projected light beam will carry OAM at the far field cross section.

A fundamental step for the design of the eight-waveguides at octagonal lattice is to model light propagation inside it. We present here a brief theoretical discussion of the coupled mode theory for eight waveguides that have different characteristics.

Under the assumption of weak coupling between the waveguides, in which the guiding regions are not too close to one another, the modes of the device can be considered as a linear combination of the modes of eight separated waveguides, each of them guiding a single mode, we further treat the electromagnetic field as scalar as we discussed in section 4.2. We can expand Equation (4.6) to consider all the waveguides and to model their propagation within our device:

$$\frac{d\mathbf{A}}{dz} = -jM(z)\mathbf{A}(z) \quad (5.1)$$

Where:

$$\mathbf{A}(z) = [A_1(z) A_2(z) \dots A_8(z)]^T$$

Defining the coupling coefficients between the i -th waveguides k_{ij} and the detuning factors $\Delta\beta_i$. The matrix M reads as follows:

$$M(z) = \begin{bmatrix} \Delta\beta_1 & k_{12} & k_{13} & & k_{18} \\ k_{21} & \Delta\beta_2 & k_{23} & \dots & k_{28} \\ k_{31} & k_{33} & \Delta\beta_3 & & k_{38} \\ & \vdots & & \ddots & \vdots \\ k_{81} & k_{82} & k_{83} & \dots & \Delta\beta_8 \end{bmatrix} \quad (5.2)$$

The coupling coefficient $k_{ij}(d)$ as a function of the interaction distance between the adjacent waveguides that are placed at the vertices of the octagonal shape. For the detuning factors

$\Delta\beta_i = C\Delta V_i$: The field and the power at the output could be written as a function of the interaction length between the waveguides as follows:

$$A(z) = A_0 e^{-jM(z)z} \quad (5.3)$$

$$P_i = |A(z)|^2 \quad (5.4)$$

Where P_i is the output power of the i -th waveguide that is placed at the vertices of the octagonal cross section.

In our case, we have simulated the device with different applicable conditions using the weakly coupled approximation theory and relying on the information we have from the previous chapter about the detuning factor $\Delta\beta$ and the coupling coefficient $k_{ij}(d)$ (Figure 5.2).

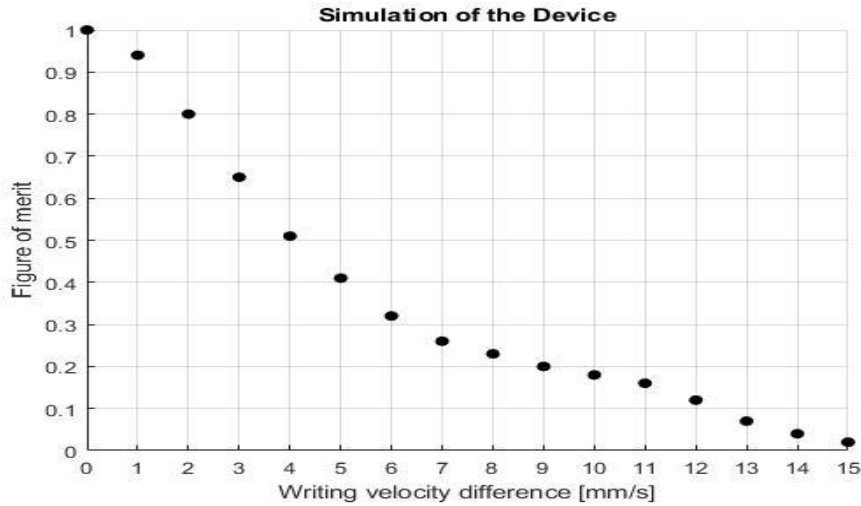


Figure 5.2: Simulation of the device's figure of merit as function of the writing velocity difference ΔV .

5.3. Fabrication of the devices

The fabrication of the final devices was performed based on the geometrical layout designs in the previous section, where the device consists of eight arms (single mode waveguide) placed at the vertices of an octagonal cross section following the arrangement of their positions (Figure 5.1). These waveguides have been fabricated into two series (say, the odd waveguides and the even waveguides). The even waveguides are fabricated with the so-called reference writing velocity (15 mm/s), while the odd waveguides are fabricated with a different writing velocity. We proceeded with the fabrication and characterization of eleven devices from two different groups. The two groups of devices were designed and fabricated to explore the waveguides coupling at the octagonal cross section configuration. First devices based on the geometrical shape of the octagonal cross section, by varying the interaction distance d that tunes the coupling coefficient k . Second devices based on the waveguide's characteristics, by varying the writing velocity difference ΔV .

First Group of Devices

Four different devices were fabricated, having a fixed interaction length $L = 2\text{mm}$ at the region of our interest and a fixed interaction distance $d = 6.6\ \mu\text{m}$ that results from a fixed radius $R = 10\ \mu\text{m}$ of the octagonal shape. Furthermore, the even and odd waveguides of each device have been inscribed as in the following table:

Device N.	V_{even} [mm/s]	V_{odd} [mm/s]	$\Delta\beta$ [mm ⁻¹]
D1	15	15	0
D2	19	15	3.4
D3	22	15	5.8
D4	25	15	8.7

Table 5.1: The waveguide's parameters for the fabrication, where each device has a set of odd and even waveguides that fabricated within different writing velocity.

As a result of the writing velocity difference between the even and odd waveguides, we have a set of detuning factors $\Delta\beta = C\Delta V$.

Second Group of Devices

Seven different devices were fabricated, having a fixed interaction length $L = 2\text{mm}$ at the region of our interest and a fixed writing velocity difference $\Delta V = 10\ \text{mm/s}$ between the even and odd waveguides. Furthermore, the interaction distance d between the waveguides at the vertices of the octagonal shape varies from $7.2\ \mu\text{m}$ to $6\ \mu\text{m}$. As a result, the coupling coefficient is changing as well. The used parameters are illustrated in Table 5.2 as follows:

Device N.	d [μm]	R_{oct} [μm]	V_{even} [mm/s]	V_{odd} [mm/s]
D1	6	8.5	25	15
D2	6.2	8.8	25	15
D3	6.4	9.1	25	15
D4	6.6	9.3	25	15
D5	6.8	9.6	25	15
D6	7	9.9	25	15
D7	7.2	10.2	25	15

Table 5.2: Geometrical structure of the regular octagonal cross section, and the writing velocity of the fabricated devices for the even and odd waveguides.

5.4. Characterization of the Devices

A preliminary characterization was performed on the final devices based on computing the figure of merit of the arms. The figure of merit represents the ratio of power that was transmitted to the other arms to the input power of the device, defined as follows:

$$\text{Figure of merit} = \frac{\sum_{i=1}^8 P_{out,i} - P_{out,j}}{\sum_{i=1}^8 P_{out,i}} \quad (5.5)$$

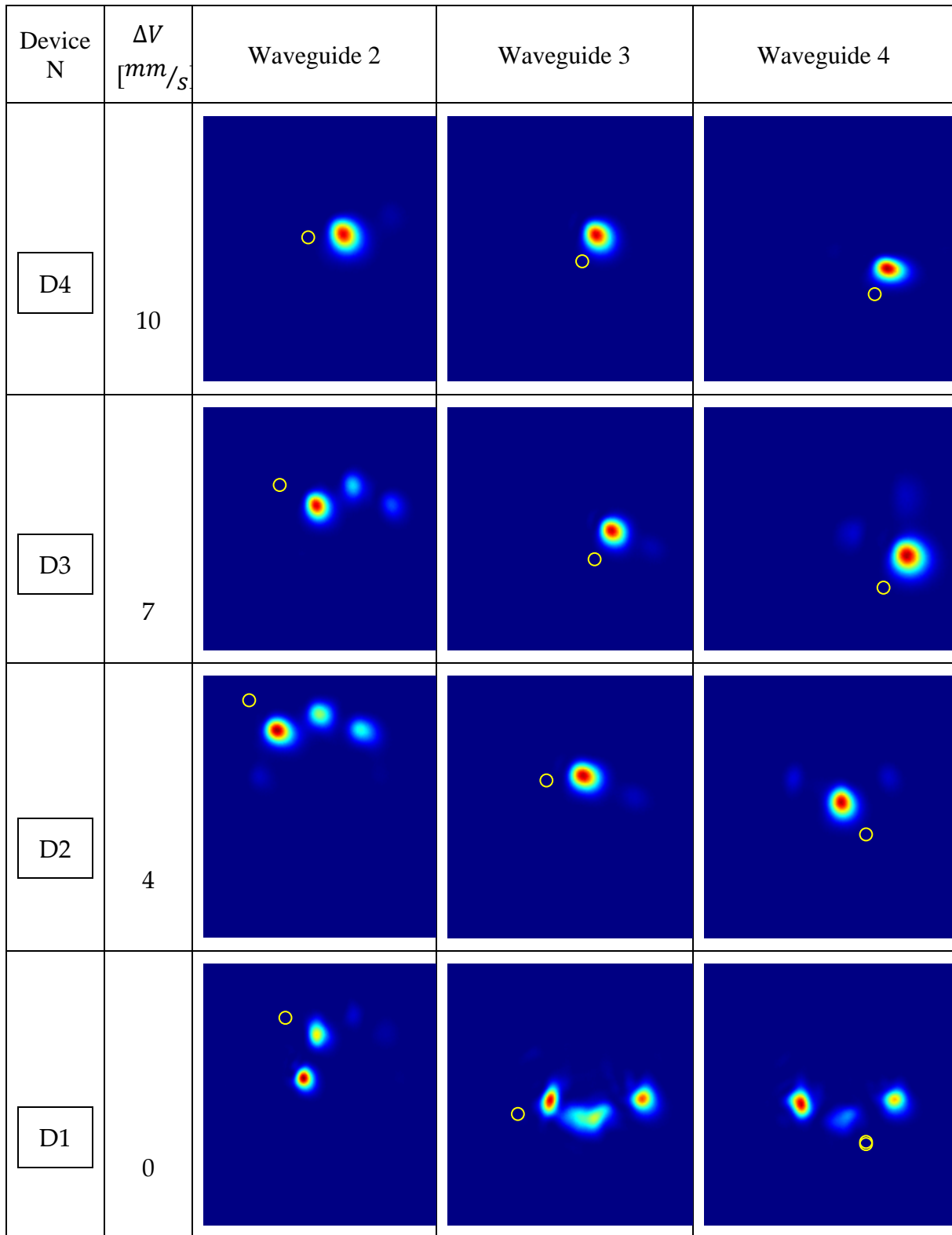
The nominator represents the summation of the output power of each waveguide of our device except the illuminated waveguide, and the denominator is the summation of the output power of each arm.

The characterization is carried out using the manual manipulator setup of the CCD camera presented in Section 3.3.2 with an 808 nm wavelength.

The modes of the waveguide in the octagonal shape were imaged with CCD property software. Make sure that the intensities of each mode profile do not saturate the sensitive pixels.

The devices are characterized by entering in three inputs (waveguide 2, 3, and 4). The acquired images from the CCD camera are reported in Table 5.3. The acquired image of each device was cropped to form an independent matrix. The peak intensity's value was represented by the maximum value in the matrix. The extracted values from each arm were used to calculate the figure of merit following Equation (5.5).

(A)



(B)

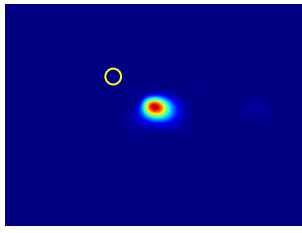
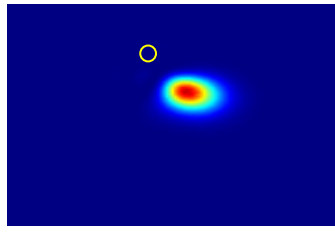
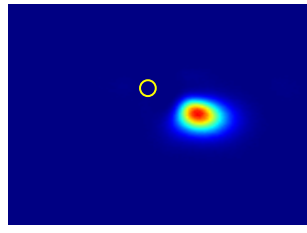
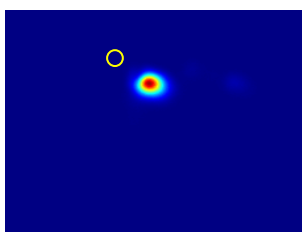
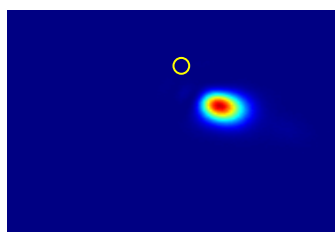
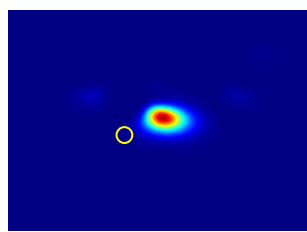
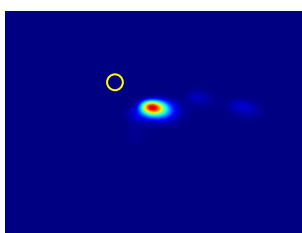
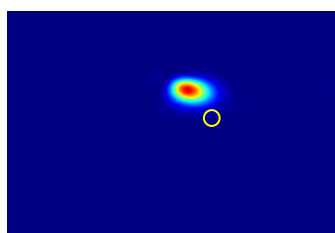
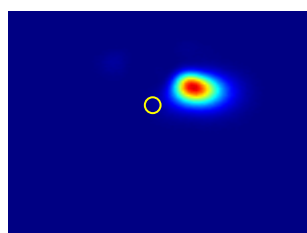
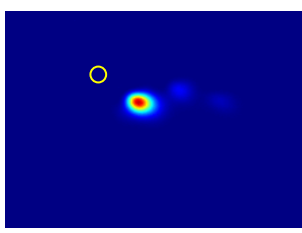
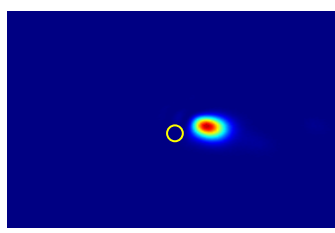
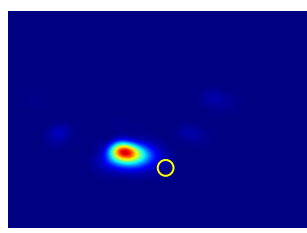
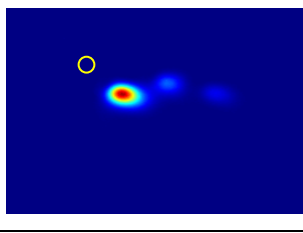
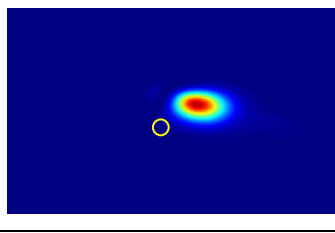
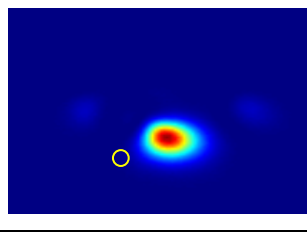
Device N	d [μm]	Waveguide 2	Waveguide 3	Waveguide4
D5	6.8			
D4	6.6			
D3	6.4			
D2	6.2			
D1	6			

Table 5.2: (A) and (B) represents the acquired images form CCD camera for first and second group of devices respectively. The device's waveguides (2, 3, and 4) that placed at the vertices of the octagonal cross section are characterized as function of ΔV and d respectively.

First group characterization

The characterization is performed over three different waveguides, where the illuminated waveguide is indicated with an orange circle in the images on Table 5.3. Figure 5.2 shows how the figure of merit decreased as the writing velocity difference increased. It is clear that the figure of merit is different for each arm. This inconsistency may appear due to the difference in the coupling between the waveguides in the octagonal cross-section, but at higher writing velocity difference the figure of merit is very low for all arms of the device.

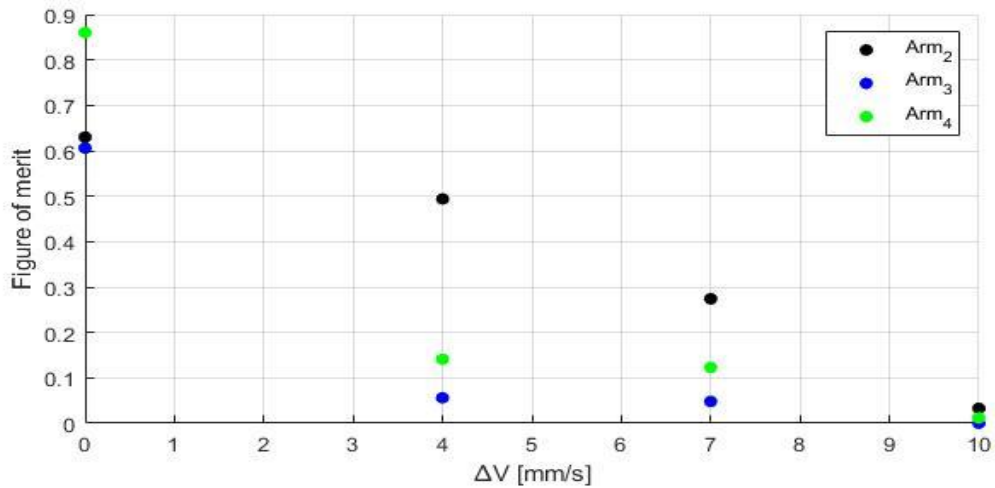


Figure 5.2: Measured figure of merit as function of the writing velocity difference ΔV . Three waveguides of our device are characterized.

Second group characterization

The experimental data shows an oscillatory decay of the figure of merit with the increase of the interaction distance d ; see Figure 5.2, in which it is qualitatively similar to the one we observed during the characterization of the detuning factor in Section 4.5. When the interaction distance d is higher than 7.2 μm the figure of merit of the three arms are identical.

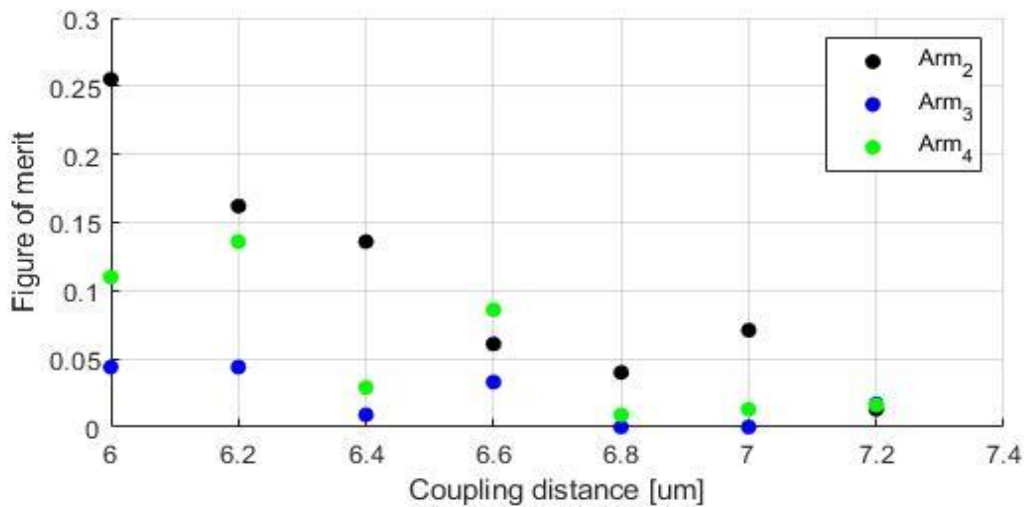


Figure 5.3: The measured figure of merits as function of the interaction distance d , where only three waveguides of our device are characterized.

The experimental results of the two types of the device show promising behaviors that can allow us to realize the final device as it was discussed in Section 2.5.

6 Conclusion

In this thesis work, we reported and discussed a device that transforms eight waveguides from a planar configuration to a two-dimensional polygonal cross-section. In particular, the output waveguides are placed at the vertices of a regular octagon. The device was fabricated by exploiting the unique three-dimensional capabilities of femtosecond laser micromachining.

The device consists of single-mode optical waveguides working at 808 nm wavelength, inscribed in alumino-borosilicate glass (Eagle XG). Laser writing parameters were experimentally optimized to obtain low propagation loss (0.5 dB/cm), good coupling with optical fibers less than 0.1dB coupling loss and reasonable curvature radii (negligible additional loss for $R > 45mm$).

In the final device, the parasitic coupling among the waveguides was quenched by controlling the propagation constant of the waveguides in the region where they are brought close together to produce the final octagonal structure, which is achieved by varying their writing velocity. The odd waveguides are written with the reference writing velocity (15 mm/s), and the detuning factor is defined as a function of the even waveguide's writing velocity.

We demonstrated devices where more than 95% of the input power remained in the same waveguide while the interaction distance was as low as 6.6 μm between the waveguides. We observed, from the results of the characterization of three different arms of the device, that there is an inconsistency in the coupling among the arms. The interpretation of this asymmetric coupling between the waveguides can be attributed to the variation of the coupling as a function of the geometrical angle.

Future work could be devoted to controlling the coupling behaviors of the device's arms at different depths, as a function of the coupling angle to improve the device symmetry.

A full device to convert the encoded qubits into OAM encoded ones could be realized by combining the results of this thesis with the results of devices discussed at the state of the art.

As a final comment one can observe that the output mode carrying OAM could be projected in the free space or coupled to a waveguiding structure, a special ring core fiber.

Bibliography

- [1]. Fox, A. M., & Fox, M. (2006). *Quantum optics: an introduction* (Vol. 15). Oxford university press.
- [2]. Yao, A. M., & Padgett, M. J. (2011). Orbital angular momentum: origins, behavior and applications. *Advances in optics and photonics*, 3(2), 161-204.
- [3]. Crespi, A., & Bragheri, F. (2016). Projecting light beams with 3D waveguide arrays. *Journal of Physics B: Atomic, Molecular and Optical Physics*, 50(1), 014002.
- [4]. Padgett, M. J. (2017). Orbital angular momentum 25 years on. *Optics express*, 25(10), 11265-11274.
- [5]. Flamini, F., Spagnolo, N., & Sciarrino, F. (2018). Photonic quantum information processing: a review. *Reports on Progress in Physics*, 82(1), 016001.
- [6]. Wang, J., Sciarrino, F., Laing, A., & Thompson, M. G. (2020). Integrated photonic quantum technologies. *Nature Photonics*, 14(5), 273-284.
- [7]. Gattass, R. R., & Mazur, E. (2008). Femtosecond laser micromachining in transparent materials. *Nature photonics*, 2(4), 219-225
- [8]. Taballione, C., van der Meer, R., Snijders, H. J., Hooijschuur, P., Epping, J. P., de Goede, M., ... & Renema, J. J. (2021). A universal fully reconfigurable 12-mode quantum photonic processor. *Materials for Quantum Technology*, 1(3), 035002.
- [9]. Lundeen, J. S., Feito, A., Coldenstrodt-Ronge, H., Pregnell, K. L., Silberhorn, C., Ralph, T. C., ... & Walmsley, I. A. (2009). Tomography of quantum detectors. *Nature Physics*, 5(1), 27-30.
- [10]. Erhard, M., Fickler, R., Krenn, M., & Zeilinger, A. (2018). Twisted photons: new quantum perspectives in high dimensions. *Light: Science & Applications*, 7(3), 17146-17146.
- [11]. Sheridan, L., & Scarani, V. (2010). Security proof for quantum key distribution using qudit systems. *Physical Review A*, 82(3), 030301.

- [12]. Cozzolino, D., Da Lio, B., Bacco, D., & Oxenløwe, L. K. (2019). High-dimensional quantum communication: benefits, progress, and future challenges. *Advanced Quantum Technologies*, 2(12), 1900038.
- [13]. Padgett, M. J. (2017). Orbital angular momentum 25 years on. *Optics express*, 25(10), 11265-11274.
- [14]. Poynting, J. H. (1909). The wave motion of a revolving shaft, and a suggestion as to the angular momentum in a beam of circularly polarised light. *Proceedings of the Royal Society of London. Series A, Containing Papers of a Mathematical and Physical Character*, 82(557), 560-567.
- [15]. Courtial, J., Dholakia, K., Allen, L., & Padgett, M. J. (1997). Gaussian beams with very high orbital angular momentum. *Optics communications*, 144(4-6), 210-213.
- [16]. Tamm, C. (1988). Frequency locking of two transverse optical modes of a laser. *Physical Review A*, 38(11), 5960.
- [17]. Nye, J. F., & Berry, M. V. (1974). Dislocations in wave trains. In *A Half-Century of Physical Asymptotics and Other Diversions: Selected Works by Michael Berry* (pp. 6-31).
- [18]. Mirhosseini, M., Magana-Loaiza, O. S., Chen, C., Rodenburg, B., Malik, M., & Boyd, R. W. (2013). Rapid generation of light beams carrying orbital angular momentum. *Optics express*, 21(25), 30196-30203.
- [19]. Yu, Y. F., Fu, Y. H., Zhang, X. M., Liu, A. Q., Bourouina, T., Mei, T., ... & Tsai, D. P. (2010). Pure angular momentum generator using a ring resonator. *Optics Express*, 18(21), 21651-21662.
- [20]. Guan, B., Scott, R. P., Qin, C., Fontaine, N. K., Su, T., Ferrari, C., ... & Yoo, S. J. B. (2014). Free-space coherent optical communication with orbital angular momentum multiplexing/demultiplexing using a hybrid 3D photonic integrated circuit. *Optics express*, 22(1), 145-156.
- [21]. Engin, E. et al. Photon pair generation in a silicon micro-ring resonator with reverse bias enhancement. *Opt. Express* **21**, 27826–27834 (2013).
- [22]. Spring, J. B. et al. Chip-based array of near-identical, pure, heralded single-photon sources. *Optica* **4**, 90–96 (2017)
- [23]. Lu, X. et al. Chip-integrated visible-telecom entangled photon pair source for quantum communication. *Nat. Phys.* **15**, 373–381 (2019).
- [24]. Vivien L and Pavesi L 2013 *Handbook of silicon photonics* (Boca Raton, FL: CRC Press)

- [25]. Munro W J, Stephens A M, Devitt S J, Harrison K A and Nemoto K 2012 *Nat. Photon.* **6** 777–81
- [26]. Metcalf B J *et al* 2014 *Nat. Photon.* **8** 770–4
- [27]. Crespi A, Osellame R, Ramponi R, Bentivegna M, Flamini F, Spagnolo N, Viggianiello N, Innocenti L, Mataloni P and Sciarrino F 2016 *Nat. Commun.* **7** 10469
- [28]. Burgwal R, Clements W R, Smith D H, Gates J C, Kolthammer W S, Renema J J and Walmsley I A 2017 *Opt. Express* **25** 28236–45
- [29]. Caruso, F., Crespi, A., Ciriolo, A. G., Sciarrino, F. & Osellame, R. Fast escape of a quantum walker from an integrated photonic maze. *Nat. Commun.* **7**, 1682 (2016).
- [30]. Santagati, R. *et al*. Witnessing eigenstates for quantum simulation of Hamiltonian spectra. *Sci. Adv.* **4**, eaap9646 (2018).
- [31]. Huh, J., Guerreschi, G. G., Peropadre, B., McClean, J. R. & Aspuru-Guzik, A. Boson sampling for molecular vibronic spectra. *Nat. Photon.* **9**, 615–620 (2015).
- [32]. Spagnolo, M., Morris, J., Piacentini, S., Antesberger, M., Massa, F., Crespi, A., ... & Walther, P. (2022). Experimental photonic quantum memristor. *Nature Photonics*, *16*(4), 318-323.
- [33]. Harris, N. C., Steinbrecher, G. R., Prabhu, M., Lahini, Y., Mower, J., Bunandar, D., ... & Englund, D. (2017). Quantum transport simulations in a programmable nanophotonic processor. *Nature Photonics*, *11*(7), 447-452.
- [34]. Gerrits, T., Thomas-Peter, N., Gates, J. C., Lita, A. E., Metcalf, B. J., Calkins, B., ... & Nam, S. W. (2011). On-chip, photon-number-resolving, telecommunication-band detectors for scalable photonic information processing. *Physical Review A*, *84*(6), 060301.
- [35]. Vaity, P., & Rusch, L. (2015). Perfect vortex beam: Fourier transformation of a Bessel beam. *Optics letters*, *40*(4), 597-600.
- [36]. Rojas-Rojas, S., Cañas, G., Saavedra, G., Gómez, E. S., Walborn, S. P., & Lima, G. (2021). Evaluating the coupling efficiency of OAM beams into ring-core optical fibers. *Optics Express*, *29*(15), 23381-23392.
- [37]. García-García, J., Rickenstorff-Parrao, C., Ramos-García, R., Arrizón, V., & Ostrovsky, A. S. (2014). Simple technique for generating the perfect optical vortex. *Optics letters*, *39*(18), 5305-5308.
- [38]. Brunet, C., Vaity, P., Messaddeq, Y., LaRochelle, S., & Rusch, L. A. (2014). Design, fabrication and validation of an OAM fiber supporting 36 states. *Optics express*, *22*(21), 26117-26127.

- [39]. Chen, M., Mazilu, M., Arita, Y., Wright, E. M., & Dholakia, K. (2013). Dynamics of microparticles trapped in a perfect vortex beam. *Optics letters*, 38(22), 4919-4922.
- [40]. Wang, F., Erhard, M., Babazadeh, A., Malik, M., Krenn, M., & Zeilinger, A. (2017). Generation of the complete four-dimensional Bell basis. *Optica*, 4(12), 1462-1467.
- [41]. Erhard, M., Malik, M., Krenn, M., & Zeilinger, A. (2018). Experimental greenberger–horne–zeilinger entanglement beyond qubits. *Nature Photonics*, 12(12), 759-764.
- [42]. Zhang, Y., Roux, F. S., Konrad, T., Agnew, M., Leach, J., & Forbes, A. (2016). Engineering two-photon high-dimensional states through quantum interference. *Science advances*, 2(2), e1501165.
- [43]. Franson, J. D. (1989). Bell inequality for position and time. *Physical review letters*, 62(19), 2205.
- [44]. Islam, N. T., Lim, C. C. W., Cahall, C., Kim, J., & Gauthier, D. J. (2017). Provably secure and high-rate quantum key distribution with time-bin qudits. *Science advances*, 3(11), e1701491.
- [45]. Martin, A., Guerreiro, T., Tiranov, A., Designolle, S., Fröwis, F., Brunner, N., ... & Gisin, N. (2017). Quantifying photonic high-dimensional entanglement. *Physical review letters*, 118(11), 110501.
- [46]. Jin, R. B., Shimizu, R., Fujiwara, M., Takeoka, M., Wakabayashi, R., Yamashita, T., ... & Sasaki, M. (2016). Simple method of generating and distributing frequency-entangled qudits. *Quantum Science and Technology*, 1(1), 015004.
- [47]. Żukowski, M., Zeilinger, A., & Horne, M. A. (1997). Realizable higher-dimensional two-particle entanglements via multiport beam splitters. *Physical Review A*, 55(4), 2564.
- [48]. Cozzolino, D., Polino, E., Valeri, M., Carvacho, G., Bacco, D., Spagnolo, N., ... & Sciarrino, F. (2019). Air-core fiber distribution of hybrid vector vortex-polarization entangled states. *Advanced Photonics*, 1(4), 046005.
- [49]. Guo, Y., Hu, X. M., Liu, B. H., Huang, Y. F., Li, C. F., & Guo, G. C. (2018). Experimental realization of path-polarization hybrid high-dimensional pure state. *Optics Express*, 26(22), 28918-28926.
- [50]. Cover, T. M. (1999). *Elements of information theory*. John Wiley & Sons.
- [51]. Liu, Z., & Fan, H. (2009). Decay of multiqubit entanglement. *Physical Review A*, 79(6), 064305.

- [52]. Davis, K. M., Miura, K., Sugimoto, N., & Hirao, K. (1996). Writing waveguides in glass with a femtosecond laser. *Optics letters*, 21(21), 1729-1731.
- [53]. Meany, T., Biggerstaff, D. N., Broome, M. A., Fedrizzi, A., Delanty, M., Steel, M. J., ... & Withford, M. J. (2016). Engineering integrated photonics for heralded quantum gates. *Scientific reports*, 6(1), 1-8.
- [54]. Gattass, R. R., & Mazur, E. (2008). Femtosecond laser micromachining in transparent materials. *Nature photonics*, 2(4), 219-225.
- [55]. Della Valle, G., Osellame, R., & Laporta, P. (2008). Micromachining of photonic devices by femtosecond laser pulses. *Journal of Optics A: Pure and Applied Optics*, 11(1), 013001.
- [56]. Osellame, R., Cerullo, G., & Ramponi, R. (Eds.). (2012). *Femtosecond laser micromachining: photonic and microfluidic devices in transparent materials (Vol. 123)*. Berlin: Springer.
- [57]. Johnston, T. F. (1998). Beam propagation (M²) measurement made as easy as it gets: the four-cuts method. *Applied optics*, 37(21), 4840-4850.
- [58]. Arriola, A., Gross, S., Jovanovic, N., Charles, N., Tuthill, P. G., Olaizola, S. M., ... & Withford, M. J. (2013). Low bend loss waveguides enable compact, efficient 3D photonic chips. *Optics express*, 21(3), 2978-2986.
- [59]. Eaton, S. M., Zhang, H., Herman, P. R., Yoshino, F., Shah, L., Bovatsek, J., & Arai, A. Y. (2005). Heat accumulation effects in femtosecond laser-written waveguides with variable repetition rate. *Optics express*, 13(12), 4708-4716.
- [60]. He, J., Xu, B., Xu, X., Liao, C., & Wang, Y. (2021). Review of femtosecond-laser-inscribed fiber bragg gratings: Fabrication technologies and sensing applications. *Photonic Sensors*, 11(2), 203-226.
- [61]. Le Camus, A., Petit, Y., Bérubé, J. P., Bellec, M., Canioni, L., & Vallée, R. (2021). Direct-laser-written integrated mid-IR directional couplers in a BGG glass. *Optics Express*, 29(6), 8531-8541.
- [62]. Kowalevich, A. M., Sharma, V., Ippen, E. P., Fujimoto, J. G., & Minoshima, K. (2005). Three-dimensional photonic devices fabricated in glass by use of a femtosecond laser oscillator. *Optics letters*, 30(9), 1060-1062.
- [63]. Wang, J., Yang, J. Y., Fazal, I. M., Ahmed, N., Yan, Y., Huang, H., ... & Willner, A. E. (2012). Terabit free-space data transmission employing orbital angular momentum multiplexing. *Nature photonics*, 6(7), 488-496.
- [64]. Bowman, R. W., & Padgett, M. J. (2013). Optical trapping and binding. *Reports on Progress in Physics*, 76(2), 026401.

- [65]. Vallone, G., D'Ambrosio, V., Sponselli, A., Slussarenko, S., Marrucci, L., Sciarrino, F., & Villoresi, P. (2014). Free-space quantum key distribution by rotation-invariant twisted photons. *Physical review letters*, 113(6), 060503.
- [66]. Guan, B., Scott, R. P., Qin, C., Fontaine, N. K., Su, T., Ferrari, C., ... & Yoo, S. J. B. (2014). Free-space coherent optical communication with orbital angular, momentum multiplexing/demultiplexing using a hybrid 3D photonic integrated circuit. *Optics express*, 22(1), 145-156.
- [67]. Crespi, A. (2015). Suppression laws for multiparticle interference in Sylvester interferometers. *Physical Review A*, 91(1), 013811.
- [68]. Reck, M., Zeilinger, A., Bernstein, H. J., & Bertani, P. (1994). Experimental realization of any discrete unitary operator. *Physical review letters*, 73(1), 58.
- [69]. Ceccarelli, F., Atzeni, S., Prencipe, A., Farinaro, R., & Osellame, R. (2019). Thermal phase shifters for femtosecond laser written photonic integrated circuits. *Journal of Lightwave Technology*, 37(17), 4275-4281.
- [70]. Crespi, A., Osellame, R., Ramponi, R., Brod, D. J., Galvao, E. F., Spagnolo, N., ... & Sciarrino, F. (2013). Integrated multimode interferometers with arbitrary designs for photonic boson sampling. *Nature photonics*, 7(7), 545-549.
- [71]. Shen, W. G., Chen, Y., Wang, H. M., & Jin, X. M. (2022). OAM mode conversion in a photonic chip. *Optics Communications*, 507, 127615.
- [72]. Chen, Y., Gao, J., Jiao, Z. Q., Sun, K., Shen, W. G., Qiao, L. F., ... & Jin, X. M. (2018). Mapping twisted light into and out of a photonic chip. *Physical review letters*, 121(23), 233602.
- [73]. Weber, K., Hütt, F., Thiele, S., Gissibl, T., Herkommer, A., & Giessen, H. (2017). Single mode fiber based delivery of OAM light by 3D direct laser writing. *Optics express*, 25(17), 19672-19679.
- [74]. Gloge, D. (1972). Bending loss in multimode fibers with graded and ungraded core index. *Applied optics*, 11(11), 2506-2513.
- [75]. Szameit, A., Dreisow, F., Pertsch, T., Nolte, S., & Tünnermann, A. (2007). Control of directional evanescent coupling in fs laser written waveguides. *Optics express*, 15(4), 1579-1587.
- [76]. Gowind P. Agrawal, *Fiber-optic communication systems*, Editore: John Wiley & Sons, Inc., Anno edizione: 2002, ISBN: 0-471-22114-7

List of Figures

Figure 1.1: A helical phase front of OAM.....	10
Figure 1.2: Spin Angular Momentum with circularly polarized field (right) carries SAM.	10
Figure 1.3: Spatial light modulator to generate OAM beam with helical phase	11
Figure 1.4: Ring resonator to generate OAM.	12
Figure 1.5: Simulation of SMW of 8 waveguides in a vertices of octagonal lattice	13
Figure 1.6: A representation of RCF,	13
Figure 1.7: The Bessel function of order of l	15
Figure (1.8): (left) first kind of the modified Bessel function of order of l	16
Figure 1.9: (a) The transvers profile of the LG modes. (b) the PV beam.	17
Figure 1.10: Hong-Ou-Mandel interferometer.	18
Figure 2.1: Femtosecond Laser Micromachining incident on dielectric material	25
Figure 2.2: Schematic representation of the nonlinear processes	27
Figure 2.3: Waveguide diameters as a function of writing velocity and repetition rates.	29
Figure 2.4: Temperature profile of the annealing process.	30
Figure 2.6: Directional coupler of coupling length	31
Figure 2.7: Representation of the geometrical shape of 1×3 beam splitter	32
Figure 2.8: Integrated circuit comprises five modes, with directional couplers and phase-shifters..	32
Figure 2.9: structure of integrated interferometers.	33
Figure 2.10: 3D section of a reconfigurable MZI, in which act as thermal shifter.	34
Figure 2.11: Representation of femtosecond laser written waveguides.	35
Figure 2.12: A representation of a single mode fiber that delivering OAM beam.	35
Figure 2.13: Distributions of the waveguides on the vertices of an octagonal shape.....	37
Figure 3.1. The representation of the femtosecond laser setup	38
Figure 3.2: Representation of end-fire fiber waveguide coupling	40
Figure 4.1: IL as function of the irradiation power.	44
Figure 4.2: CL [dB] and PL [dB/cm] of femtosecond laser written waveguides	45
Figure 4.3: Bending Losses of femtosecond laser written waveguides.....	46
Figure 4.4: The transmissivity as function of the coupling distance d . (b)	50
Figure 4.5: The transmissivity of the directional couplers as a function of the writing velocity.	52

Figure 5.1: Geometrical configuration of the final device	53
Figure 5.2: Simulation of the device's figure of merit	55
Table 5.2: Acquired images form CCD camera for first and second group of devices.....	59
Figure 5.2: Measured figure of merit as function of the writing velocity difference ΔV	60
Figure 5.3: The measured figure of merits as function of the interaction distance d.	60

List of Tables

Table 4.1: The ILs, CLs, and PLs of the optimal waveguides.	46
Table 5.1: The waveguide's parameters for the fabrication of the final device.....	56
Table 5.2: Geometrical structure of the regular octagonal cross section	56
Table 5.2: Acquired images of the final devices with CCD camera.	59

Acknowledgments

At the end of this journey, I would first like to thank Professor Roberto Osellame for welcoming me into his research group and giving me the opportunity to work on this thesis project. A special thanks must go to Dr. Andrea Crespi, for his infinite patience and for all the discussions from which I learned a lot about how to approach problems and how to approach life in the lab. He was always enthusiastic about helping me solve any kind of problem.

I would also like to thank Riccardo Albiero for helping me take my first steps in the laboratory, Simone Atzini, and all the other people with whom I shared these days.

I would like to send a special thank to our big family of Lecoo city who shared with me all the funny and eventful time.

Finally, I want to thank all members of Ahmed Siddig's family for the encouragement and support they have given me through out these tough years.

